Luminescence dating at Border Cave: attempts, questions, and new results

Chantal Tribolo, Norbert Mercier, Charles Dumottay, Nadia Cantin, William E. Banks, Dominic Stratford, Paloma de la Peña, Lucinda Backwell, Lyn Wadley, Francesco D'errico

Luminescence dating at Border Cave: attempts, questions, and new results

Chantal Tribolo[a *], Norbert Mercier[a], Charles Dumottay[a], Nadia Cantin[a], William E. Banks[b,c], Dominic Stratford[d], Paloma de la Peña[e, f, g], Lucinda Backwell[g, h, i], Lyn Wadley[g], Francesco d'Errico[b, j]

[a] *Archéosciences Bordeaux, CNRS - Bordeaux Montaigne University, Esplanade des Antilles 33607 Pessac, France.*

[b] *University of Bordeaux, CNRS, MCC, PACEA, UMR 5199, Allée Geoffroy Saint Hilaire, CS 50023, F - 33615, Pessac CEDEX, Talence, France.*

[c] *Biodiversity Institute, University of Kansas, Lawrence, KS, 66045-7562, USA*

[d] *School of Geography, Archaeology and Environmental Studies, University of the Witwatersrand, Private Bag 3, WITS, 2050, South Africa.*

[e] *Departamento de Prehistoria y Arqueología, Facultad de Filosofía y Letras. Campus Universitario de Cartuja s/n, 18071. Universidad de Granada, Spain.*

[f] *McDonald Institute for Archaeological Research, University of Cambridge, Downing Street, Cambridge CB2 3ER, United Kingdom.*

[g] *Evolutionary Studies Institute, University of the Witwatersrand, Private Bag 3, WITS, 2050, South Africa.*

[h] *Centre of Exploration for the Deep Human Journey, University of the Witwatersrand, Private Bag 3, WITS, 2050, South Africa.*

[i] *Instituto Superior de Estudios Sociales (ISES-CONICET), San Lorenzo 429, San Miguel de Tucumán, CP4000, Tucumán, Argentina.*

[j] *Centre for Early Sapiens Behaviour, Øysteinsgate 3, Postboks 7805, 5020, University of Bergen, Norway.*

* Corresponding author: ctribolo@u-bordeaux-montaigne.fr

Abstract

Border Cave hosts a rare Middle and Early Later Stone Age sequence of deposits that extends as far back as ca. 250 thousand years (ka). The site's chronology has been built mainly on Electron Spin Resonance (ESR) ages obtained from teeth, conducted at the end of the 1990s, and on radiocarbon

dating for the more recent layers. In order to refine the sequence's chronology, several materials were selected for luminescence dating, including 34 siliceous lithic artefacts, and quartz and feldspar grains extracted from 10 sediment samples. Since the radioisotopic contents of the cave sediments are abundant in the volcaniclastic host rock (about 2% K, 10 ppm ^{232}Th, 2 ppm ^{238}U in the sediments) and the ages for the lower layers are over 40 ka, high (> 150 Gy) equivalent doses (De) were expected for most samples. The saturated thermoluminescence (TL) signals of the lithic artefact samples suggested either that they had not been heated in the past, or that they were already too old to be dated. The presence in the sediments of 40 - 63 µm quartz grains dominated by the fast Optically Stimulated Luminescence (OSL) component and with apparent high D_0 values (200 - 1000 Gy) suggested, *a priori*, that they could be appropriate for measuring high De_s. However, a systematic drop of the De values for these high D_0 grains was observed and could not be fully understood and corrected accordingly. The recently proposed pIT protocol, together with a global growth curve (GGC) approach, was applied to 63 - 80 µm feldspar grains extracted from the sediment samples. The data suggest that the IR225 signal was likely not fully bleached at the time of deposition. Nonetheless, two age estimates, assumed to bracket the target age, have been calculated for each sample. These estimates are consistent with the previous ESR ages and the ESR/C14-based Bayesian models. Further improvements can be considered in the future with the pIT - GGC method, which would allow both increased accuracy and precision.

1. Introduction

Border Cave is one of the few sites in southern Africa that hosts a long Middle and Early Later Stone Age (ELSA) sequence of deposits, and from which cultural, environmental and human remains from the last 250 thousand years (ka) have been recovered. It was first excavated by Raymond Dart in 1934, and subsequently by Malan, Cooke and Wells in 1941-1942, following the discovery by Horton of human remains during fertilizer extraction. Peter Beaumont conducted extensive excavations during the 1970s and 1980s (Beaumont et al. 1978, Beaumont, 1980), followed recently by Backwell, d'Errico and Wadley (Backwell et al., 2018, 2022). The sequence has been described mainly as an alternating sequence of White Ash (WA) and Brown Sand (BS) deposits, numbered from 1 at the top to 6 at the bottom, encompassing Iron Age, Early Later Stone Age (ELSA), Post Howiesons Poort/MSA 3, Howiesons Poort/MSA 2 and MSA 1 technocomplexes.

The sedimentary sequence of Border Cave was one of the first to be extensively dated by methods based on physical or chemical processes, including radiocarbon on charcoal (mainly) (Beaumont et al., 1978; Beaumont, 1980; Beaumont et al., 1992; Bird et al., 2003; Villa et al., 2012; d'Errico et al., 2012), Amino Acid Racemization (AAR) on ostrich eggshells (Miller and Beaumont, 1989; Miller et al., 1992; Miller et al., 1993; Miller et al., 1999), and U-series/Electron Spin Resonance (ESR) on teeth (Grün et al., 1990; Grün and Beaumont, 2001; Grün et al., 2003). Radiocarbon implied that the ELSA was one of the earliest currently identified in southern Africa, starting at ca. 44 ka (Beaumont and Vogel, 1972; Vogel and Beaumont, 1972). This was confirmed more recently by targeted radiocarbon dating of diagnostic artefacts (Villa et al., 2012; d'Errico et al., 2012). The lower part, from Member 2 WA, is beyond the limit of the radiocarbon method. AAR was challenging because most of the 146 tested ostrich eggshell fragments were burnt and incompatible with this method. Meanwhile Members 2 BS and 2 WA, associated with MSA 3 a and b (Beaumont's attribution), were dated to 47 ± 5 ka, 56 ± 6 and 69 ± 7 ka with the AAR method. Members 4 BS, 4 WA and 5 BS associated with MSA 1 were estimated to be older than 100 ka. Grün et al. (1990, 2001, 2003) analyzed 25 bovid teeth covering all members from 1 BS (ELSA) to 5 WA (MSA 1). Each tooth was subdivided into two or three fragments. The ESR papers from 2001 and 2003 represent successive improvements of the

measurements and age calculations initiated in 1990, so here we consider only the series published in 2003 (Grün et al., 2003). Consistent ages were obtained for most of the Upper and Middle Pleistocene, from 33 ± 1 ka to 227 ± 11 ka. A human tooth from the BC5 human mandible, discovered at the base of Member 3 WA was directly dated applying U-series/ESR, and an age of 74 ± 5 ka was obtained, in agreement with the ESR age for the 3 WA Member (64 ± 2 ka). A Bayesian model was then proposed by Millard et al. (2006) based on the ESR data, and a Bayesian model based on the radiocarbon data has also been produced (d'Errico et al., 2012).

J. Huxtable calculated eight thermoluminescence (TL) ages from lithics in the late 1980s and H. Valladas and N. Mercier obtained 16 TL ages from 216 preselected lithics in the late 1990s (Valladas, pers. comm.), which are in agreement with the other data sets, in particular with the ESR ages (Grün and Beaumont (2001), and personal observation of these data). Unfortunately, none of these ages is published. Despite optical dating of sediments being the most applied method to establish the chronology of MSA sequences (e.g. Wadley et al., 2015), no such application has yet been published for Border Cave. Here, we report one of the first complete luminescence dating studies of the Border Cave sedimentary sequence, utilizing TL on lithics, and Optically Stimulated Luminescence (OSL) on sedimentary quartz and feldspar grains. A brief report on the tests performed on 34 lithics can be found in the Supplementary Information (Table sup.1; Fig. sup.1). We show here that only the feldspar grains provide useable results. In addition, two new Bayesian models have been produced with ChronoModel software from the ESR and C14 data (see Supplementary Information Section 5; Tables sup.5, sup.6A, sup.6B). They are in agreement with the feldspar grains' chronology.

2. Site and geology

Here we give a brief description of the site setting and geology, which can be found in more detail in Backwell et al. (2018, 2022), and Stratford et al., (2022). Border Cave is 50 m wide and 35 m long. It is located 82 km west of the Indian Ocean, at 600 m.a.s.l., on a west-facing cliff of the Lebombo Mountain range overlooking the Eswatini Lowveld, 500 m below. The shelter was formed by differential erosion of the Lower Jurassic felsic extrusive rocks of the Jozini Formation. The two volcaniclastic facies of the roof and walls of Border Cave are described as clast-supported and matrix-supported breccias, which contain rhyolites, and silt- and clay-rich sandstones. The non-anthropogenic components of the sediments within the cave derive mostly from the weathering of the walls and roof, with additional clastic and chemical contributions from aeolian grains, and guano from bats and birds. The anthropogenic component of the sediments is represented by lithic artefacts, bones, seeds, land snail shells, charcoal, ash, wood, layered grass bedding, and anthropogenically introduced particles. The preservation of organic material in some layers is exceptional, suggesting that the cave was, for the most part, quite dry in the past. Evidence of moisture is attested by the sporadic presence of calcite and gypsum, two soluble precipitate minerals, whilerecent stratigraphic analysis has also revealed the presence of fluid interaction structures (Stratford et al., 2022). Post-depositional processes have variably affected the deposits and include localized anthropogenically-induced mixing through trampling or surface modification (dumping, raking of combustion features, digging of pits and combustion feature bases), and geogenic processes, such as low energy run-off, mixing and reworking of sediments laterally and vertically, localized spall accumulation deforming and fragmenting features, and ancient and modern animal burrowing.

X ray diffraction (XRD) analyses were performed at the Archeosciences Bordeaux laboratory on sediment samples from the upper units of the sequence (1 BS, 1 WA, 2 BS, 2 WA) (Table sup.2). They clearly demonstrated the presence of quartz and calco-sodium feldspar grains, with potassium feldspar

in lower quantities, as well as gypsum and/or calcite. All samples, however, are dominated by zeolites, which are low-density alumino-silicate minerals formed by the devitrification of volcanic glass and derived from the breakdown of the lithologically-variable volcaniclastic rhyolites in which the shelter is hosted.

3. Sediment samples: location and preparation

Sediment samples for OSL dating were taken from the recently exposed profiles, at night, under subdued orange light, after removing the surface of the section exposed to natural light. Although the most recent excavations provide a new interpretation of the site's stratigraphy with renamed/reinterpreted layers, we attempted to identify Beaumont's members in order to link the data from the two excavations (Backwell et al., 2022; Stratford et al., 2022). Beaumont's data and in particular the location of the teeth used for obtaining the ESR data, are well known at the member level, even though their exact numerical elevations relative to the datum point are unknown. Here we present the sediment samples within the revised member boundaries along with the cultural attribution assigned by Beaumont for each one (Grün and Beaumont, 2001; Grün et al., 2003). Note, however, that these cultural attributions probably also need to be revised (de la Peña, in press). Sediment samples BDC 1, 2, 9 and 10 come from Member 2 BS, attributed to MSA 3 (Fig. 1 and Table 1). Samples BDC 3 and 4 come from the lower part of Member 2 WA, also attributed to MSA 3. Sample BDC 5 is associated with the upper part of 4 BS or the lower part of 1 RGBS, so it is not clear whether it is associated with the Howiesons Poort or MSA 1. Samples BDC 6, 7 and 8 were taken respectively from Members 4 WA, 5 BS and 5 WA, all attributed to MSA 1. All samples, except for BDC 9 and 10, come from the northern area of the new excavation, in excavation 3A rear, while BDC 9 and 10 were taken at the top of the profile in the southern area (excavation 4A), from squares N103/E119 and N104/E118.

Table 1. Location of the 10 sediment samples dated by OSL. The cultural attributions are those tentatively given by Grün and Beaumont (2001) and will be revised in the near future.

Sample	E	N	Z	Excavation area	Member	Layer	Cultural attribution
BDC 1	119.32	109.96	104.08	northern	2 BS	Grass Mat Camilla	MSA 3
BDC 2	119.28	109.95	103.82	northern	2 BS	Yellowish Brown Caz	MSA 3
BDC 3	117.71	109.51	103.16	northern	2 WA lower	Dossy unit above combustion feature 3	MSA 3
BDC 4	118.22	109.47	103.20	northern	2 WA lower	Dossy unit above combustion feature 3	MSA 3
BDC 5	117.97	108.99	102.81	northern	1 RGBS/4 BS	Very Dark Brown Faan	HP/MSA 1
BDC 6	114.54	109.69	101.94	northern	4 WA	White Idaho	MSA 1
BDC 7	113.96	108.73	101.50	northern	5 BS	Brown John	MSA 1
BDC 8	113.95	109.49	101.43	northern	5 WA	Dark Brown Kevin	MSA 1
BDC 9	119.05	103.63	104.25	southern	2 BS	Brown Caby	MSA 1
BDC 10	118.94	104.10	104.09	southern	2 BS	Brown Caby	MSA 1

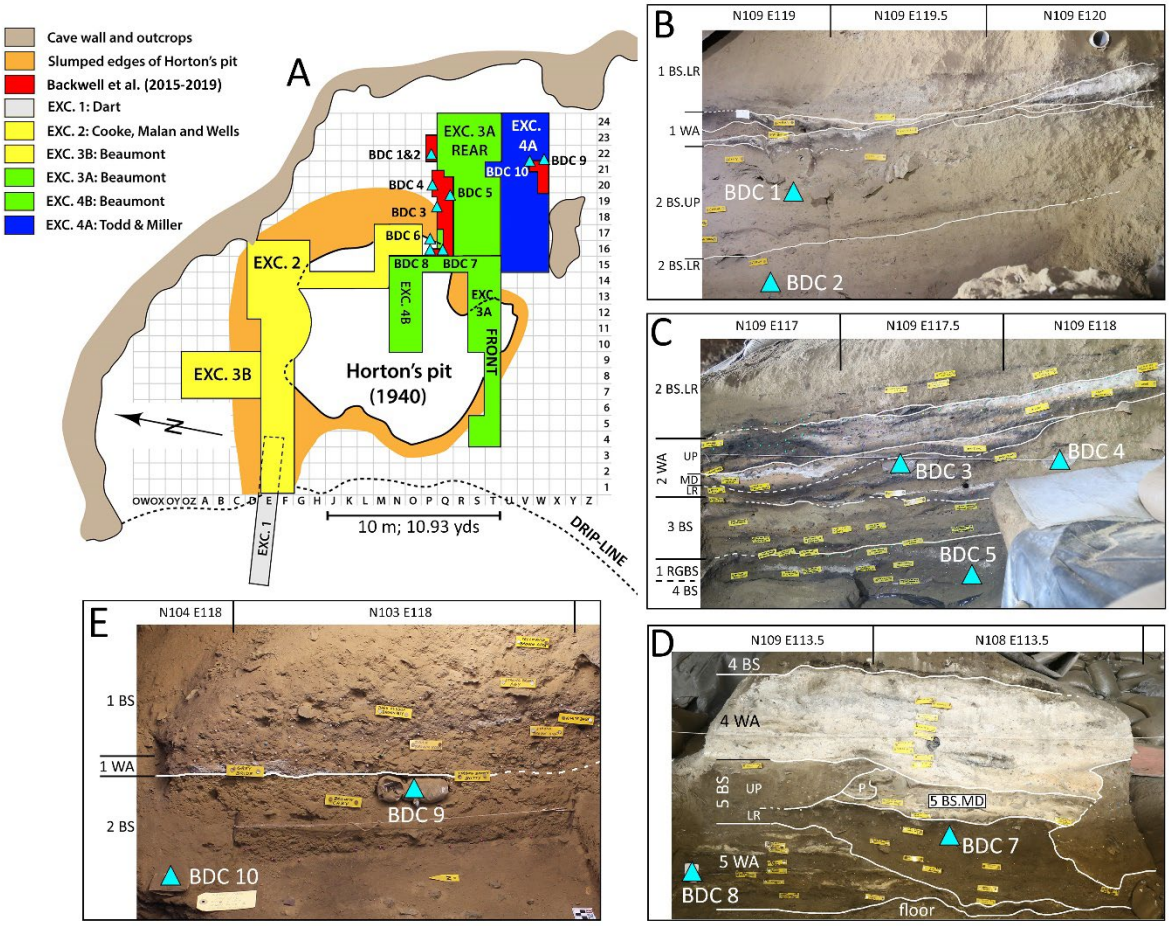

Figure 1 : Location of the ten sediment samples taken for optical dating. A) shows the location of the samples in relation to the shelter, and previous and new excavation areas, and previous excavation grid established by Cooke (1941). B-E show the stratigraphic context of the samples with new grid square names (Backwell et al., 2018); B) North profile of the current excavation (northern area) showing the location of BDC1 and BDC2; C) North profile with the location of samples BDC3, BDC4 and BDC5; D) Eastern profile displaying BDC7 and 8. BDC 6 is located in 4 WA, around the left corner, in the south profile, 50 cm east of the profile face; E) Eastern profile, from the southern excavation area (by excavation 4A) displaying samples BDC9 and 10.

First, each sample was dried and sieved with 2 mm and 1 cm mesh. The >1 cm fraction was discarded. The 2 mm - 1 cm fraction and about 20 g of the <2 mm fraction were finely crushed for gamma spectrometry analyses. They were sealed in plastic containers with wax and left for at least one month before the measurements were performed. The rest of the <2 mm fraction was processed in order to extract feldspar and quartz grains. It was wet sieved at 250 and 63 µm. The 63-250 µm and <63 µm fractions were treated with HCl (10%) for carbonate removal and H_20_2 (30%) for organic material removal. The entire <63 µm fraction was treated with H_2SiF_6 in order to retain only quartz grains, and further sieved at 20 and 40 µm. The quartz purity was checked with scanning electron microscopy-energy dispersive X-ray spectroscopy (SEM-EDS). The grains of the 63-250 µm fraction were placed successively into solutions of heteropolytungstate of sodium at densities 2.00, 2.45, 2.58, 2.62, 2.72 g/cm^3 in order to separate (from less dense to denser) zeolites, potassium feldspars, calco-sodium feldspars, quartz and heavy minerals. The 63-80, 80-200 and 200-250 µm granulometric fractions enriched in potassium feldspars were further separated with wet sieving and then dried. The supposedly quartz fraction (density 2.62-2.72) was completely dissolved after treatment with either

HF (40% for one hour, for 200-250 µm grains) or H_2SiF_6 (30%, for one week, for 100-200 µm and 63-100 µm grains), suggesting that it was not quartz but denser feldspars or unusually fragile quartz.

The 40-63 µm quartz grains and 63-80 µm potassium feldspar grains were selected for luminescence measurements.

4. Luminescence measurement devices

Most of the measurements on sedimentary quartz grains were performed on a single grain TL/OSL DA 20 reader (DTU Nutech, Bøtter-Jensen et al., 2000). The quartz grains were placed on discs containing 100 holes, each 100 µm in diameter and 100 µm deep, so that they were filled only with one or two grains. Excitation was done with a 10 mW Nd: YVO4 diode-pumped laser (532 nm) and detection was done with a PDM 9107Q-AP-TTL-02 photo-multiplier tube preceded by 7 mm Hoya U340 filter (range 280-380 nm). The reader was equipped with a $^{90}Sr/^{90}Y$ beta source delivering about 0.10 Gy/s to the quartz grains.

For the feldspar grains, a Lexsyg Smart reader was used. The 63-80 µm grains were attached to stainless steel cups with a 5 mm silicone oil impregnated pad. Excitation was done with 850 nm LEDs and detection was done with a combination of 3 mm Schott BG39 and 3.5 mm AHF Brightline HC 414/46 interference filter in front of a H7360-02 PM tube. The reader is equipped with a $^{90}Sr/^{90}Y$ beta source delivering about 0.17 Gy/s to the grains.

5. Dose rate: methods and results

Cosmic rays, alpha and beta particles and gamma rays from natural radioisotopes present in sediments and rocks, contribute to the total dose rate.

The calculation of the cosmic dose rate was based on the equation provided by Prescott and Hutton, (1994). It takes into account the geographic coordinates of the site and the density and thickness of material above the sample, the main contributor being the cave roof thickness (about 10 m, density 2.5 g/cm^3). The geometry of the cave was also considered, leading to a cosmic dose rate of 0.05 ± 0.01 Gy/ka, which was applied to all samples.

For estimating the gamma dose rate, *in situ* measurements were performed with dosimeters. Each one contained three Al_2O_3:C chips inserted in the tip of a duralumin tube (Kreutzer et al., 2018, 2020). The tubes were sunk to a depth of 30 cm into the stratigraphic sections, at the locations where the sediment samples had been extracted. They were left for over one year. The dosimeter associated with sample BDC 1 was unfortunately lost. For each dosimeter (tube) the apparent gamma dose rate increases with increased chip thickness, which was systematically recorded (Fig. sup.2), inducing a scatter of about 20% (Kreutzer et al., 2020). While this scatter could be reduced with an appropriate calibration that should be performed for each chip thickness, this one is not yet available, so a mean calibration dose rate has been applied. The deduced gamma dose rates stand between 0.96 ± 0.15 and 1.59 ± 0.11 Gy/ka and are in the same range as those measured by Grün and Beaumont (2001). For BDC1, the gamma dose rate was deduced from the radioisotopic contents of the sample (see below). This approach is less accurate than the *in situ* measurements because it does not take into account the heterogeneity of the radiation field at the centimeter scale (maximum range for gamma rays from natural radioelements is about 30 cm in sediments). However, the impact of this inaccuracy on the

final dose rate is constrained by the fact that the gamma dose rate contributes to only about 32% (mean estimated on the other samples) of the total dose rate (Table 2).

Table 2. Dose rates for the 63-80 µm feldspar grains. Beta 1 corresponds to the beta dose rate calculated from the radioisotopic contents of the fine (<2 mm) fraction, while beta 2 corresponds to the radioisotopic contents calculated from the total (<1 cm) fraction. Their mean is taken into account for the calculation of the total dose rate. The beta and alpha dose rates are corrected for water attenuation, taking into account the current moisture indicated in the second column (mass of water over mass of dry sediment). The percentage of coarse fraction in column 3 is the ratio of the mass of sediment of fraction 2 mm - 1 cm over the mass of sediment <1 cm. Uncertainties indicated here take into account both statistical and systematic uncertainties.

sample	water content	coarse fraction	dose rates (Gy/ka)											
			cosmic		gamma		beta1		beta 2		alpha		internal		total	
	(%)	(%)												
BDC 1	5%	16%	0.055	± 0.005	1.33	± 0.10	2.40	± 0.23	2.38	± 0.23	0.23	± 0.03	0.30	± 0.05	**4.30**	**± 0.26**
BDC 2	5%	22%	0.055	± 0.005	1.38	± 0.14	1.61	± 0.16	1.76	± 0.18	0.13	± 0.02	0.30	± 0.05	**3.55**	**± 0.23**
BDC 3	5%	8%	0.055	± 0.005	0.96	± 0.15	2.16	± 0.21	2.17	± 0.21	0.21	± 0.03	0.30	± 0.05	**3.69**	**± 0.26**
BDC 4	5%	13%	0.055	± 0.005	1.28	± 0.17	2.09	± 0.21	2.17	± 0.21	0.19	± 0.03	0.30	± 0.05	**3.96**	**± 0.27**
BDC 5	8%	9%	0.055	± 0.005	1.19	± 0.13	1.69	± 0.17	1.74	± 0.18	0.15	± 0.02	0.30	± 0.05	**3.42**	**± 0.22**
BDC 6	4%	14%	0.055	± 0.005	1.09	± 0.06	1.32	± 0.13	1.29	± 0.12	0.14	± 0.02	0.30	± 0.05	**2.89**	**± 0.15**
BDC 7	6%	16%	0.055	± 0.005	1.16	± 0.15	1.99	± 0.20	2.02	± 0.20	0.16	± 0.02	0.30	± 0.05	**3.68**	**± 0.26**
BDC 8	7%	12%	0.055	± 0.005	1.31	± 0.14	1.60	± 0.16	1.74	± 0.18	0.14	± 0.02	0.30	± 0.05	**3.48**	**± 0.23**
BDC 9	4%	25%	0.055	± 0.005	1.59	± 0.11	2.58	± 0.26	2.64	± 0.26	0.22	± 0.03	0.30	± 0.05	**4.78**	**± 0.29**
BDC 10	4%	14%	0.055	± 0.005	1.56	± 0.18	2.46	± 0.24	2.49	± 0.24	0.22	± 0.03	0.30	± 0.05	**4.62**	**± 0.31**

The external beta and alpha dose rates of the feldspar grains have been deduced from the radioisotopic contents of each sample, applying the conversion factors of Guérin et al. (2011), the attenuation factors of Guérin et al. (2012) for beta dose rate, or of Brennan et al. (1991) for alpha dose rate, and the alpha sensitivity correction (a-value of 0.086 ± 0.013) of Ree-Jones (1995). The radioisotopic contents of each sample were determined with high resolution gamma spectrometry (Canberra U-shaped germanium detector at low temperature).

U, Th and K activities or contents are reported in Table 3. No significant systematic disequilibrium can be detected in the U series. The activities of the coarse fractions are in most cases, except for BDC6, either consistent or up to 73 ± 5% higher (in particular for BDC2 and 8) than the ones for the fine fractions. In order to take into account auto-absorption and shielding phenomena induced by coarser materials of different radioisotopic contents, the beta dose rate was calculated on the one hand from the fine fraction, and on the other hand from the total (<1 cm) sample (Martin et al., 2015; Tribolo et al., 2017). This rate was calculated from the two activities' estimates (fine and coarse) and from the relative weight of the two fractions. The "fine" and "total" beta dose rates (beta 1 and beta 2, respectively, in Table 2) bracket the true mean beta dose rate and their mean is taken as the final estimate. For the alpha dose rate, only the activities from the fine fraction are taken into account.

Table 3. ^{238}U chain and ^{232}Th chain activities or K contents estimated from different fractions of the samples. The total (<1cm) activities and contents are calculated from the measured activities and contents for the fine (<2 mm) and coarse (2 mm - 1 cm) fractions and from the proportion of coarse material indicated in the third column of Table 2.

	sample BDC	activities (Bq/kg)								content (%)	
		^{238}U series						^{232}Th series		K	
		top		middle		bottom					
fraction <2 mm	1	37.7	± 2.7	25.6	± 0.4	32.7	± 5.1	50.1	± 0.6	2.47	± 0.04
	2	18.1	± 2.1	17.4	± 0.4	21.3	± 4.3	28.9	± 0.4	1.74	± 0.03
	3	31.3	± 3.0	27.8	± 0.5	24.0	± 5.8	45.8	± 0.6	2.19	± 0.04
	4	27.4	± 2.9	22.6	± 0.5	21.3	± 5.8	43.2	± 0.6	2.17	± 0.04
	5	23.9	± 2.5	21.4	± 0.4	23.7	± 4.9	34.5	± 0.5	1.81	± 0.03
	6	20.8	± 2.6	18.6	± 0.5	16.1	± 5.5	28.7	± 0.5	1.29	± 0.03
	7	21.8	± 2.5	21.6	± 0.5	25.2	± 5.1	35.9	± 0.5	2.18	± 0.04
	8	19.3	± 3.1	18.8	± 0.6	19.8	± 6.5	31.5	± 0.6	1.73	± 0.04
	9	29.2	± 3.1	27.4	± 0.5	18.8	± 5.8	50.2	± 0.7	2.71	± 0.05
	10	32.7	± 2.6	24.5	± 0.4	23.3	± 4.9	50.0	± 0.6	2.55	± 0.04
fraction [2mm - 1cm]	1	27.1	± 2.7	24.3	± 0.5	33.5	± 5.8	34.0	± 0.5	2.47	± 0.04
	2	29.1	± 2.8	30.1	± 0.5	27.9	± 5.7	37.1	± 0.6	2.40	± 0.04
	3	31.4	± 3.2	30.4	± 0.6	25.4	± 6.3	41.2	± 0.7	2.38	± 0.04
	4	31.7	± 1.9	29.5	± 0.4	21.1	± 4.1	42.9	± 0.5	3.00	± 0.04
	5	28.8	± 2.6	25.7	± 0.5	30.1	± 5.6	34.3	± 0.5	2.54	± 0.04
	6	13.2	± 1.9	13.7	± 0.3	9.5	± 3.9	22.6	± 0.4	1.09	± 0.02
	7	23.3	± 2.7	34.5	± 0.6	24.0	± 5.6	35.5	± 0.6	2.26	± 0.04
	8	31.2	± 3.4	29.7	± 0.6	28.5	± 6.9	42.5	± 0.7	3.15	± 0.06
	9	35.0	± 2.6	28.7	± 0.5	19.6	± 5.0	42.4	± 0.6	3.05	± 0.05
	10	32.7	± 2.9	29.6	± 0.5	25.8	± 5.7	39.1	± 0.6	2.89	± 0.05
total (< 1 cm)	1	36.0	± 2.7	25.4	± 0.4	32.8	± 5.1	47.5	± 0.6	2.47	± 0.04
	2	20.5	± 2.1	20.2	± 0.4	22.8	± 4.3	30.7	± 0.4	1.88	± 0.03
	3	31.3	± 3.0	28.0	± 0.5	24.1	± 5.8	45.4	± 0.6	2.21	± 0.04
	4	27.9	± 2.9	23.5	± 0.5	21.3	± 5.8	43.2	± 0.6	2.28	± 0.04
	5	24.4	± 2.5	21.8	± 0.4	24.3	± 4.9	34.5	± 0.5	1.88	± 0.03
	6	19.7	± 2.6	17.9	± 0.5	15.2	± 5.5	27.9	± 0.5	1.26	± 0.03
	7	22.1	± 2.5	23.7	± 0.5	25.0	± 5.1	35.8	± 0.5	2.19	± 0.04
	8	20.8	± 3.1	20.1	± 0.6	20.9	± 6.5	32.8	± 0.6	1.90	± 0.04
	9	30.6	± 3.1	27.7	± 0.5	19.0	± 5.8	48.2	± 0.7	2.79	± 0.05
	10	32.7	± 2.6	25.2	± 0.4	23.7	± 4.9	48.5	± 0.6	2.60	± 0.04

The gamma, alpha and beta dose rates must be corrected for moisture content, since water absorbs a part of the radiative energy. The moisture content of each sediment sample at the time of sampling was measured. It stands between four and seven percent (Table 2). We suggest that the moisture content in the past was likely not much higher, given that evidence of fluid presence is limited to localized minor precipitate formations, sporadic and locally constrained fluid run-off that did not lead to substrate saturation, and the preservation of desiccated organic remains (see Sievers et al., 2022 and Stratford et al., 2022). Therefore, the current water content was assumed to be representative of past mean content. The gamma dose rate from the dosimeters was then taken as such (since the *in situ* dosimeter already takes into account the impact of moisture during its burial). For alpha and beta dose rates, correction factors of Zimmerman (1971) were applied. For the 63-80 µm feldspar grains, the final beta dose rates stand between 1.30 ± 0.12 and 2.48 ± 0.24 Gy/ka, and the alpha dose rates between 0.13 ± 0.02 and 0.22 ± 0.03 Gy/ka.

For the potassium feldspar grains, an internal dose rate must also be taken into account. A mean content of 12.5 ± 2.5 % K was applied following Huntley and Baril (1997) and supplemented with 400

± 100 ppm Rb (Huntley and Hancock, 2001), resulting in an internal dose rate of 0.30 ± 0.05 Gy/ka. The internal dose rate contributes from six to ten percent of the total dose rate.

The total dose rates for the feldspar grains stand between 2.89 ± 0.15 and 4.78 ± 0.29 Gy/ka, which is higher than in most South African MSA sites.

6. Equivalent doses

Considering the high dose rates and the expected ages (>40 ka after the ESR and radiocarbon results), most of the expected equivalent doses (De) are over 150 Gy for the quartz grains, and over 180 Gy for the feldspar grains. This suggests that the De_s for quartz are likely close to saturation, thus making their determination challenging.

6.1 Quartz grains

A quartz OSL signal is known to be composed of several components, called fast, middle and slow, depending on their bleachability. The fast component is the most suitable for standard protocols, such as the single aliquot and regenerative dose protocol (SAR, Murray and Wintle, 2000). A LM-OSL (linearly modulated OSL) test was conducted on the 40-63 µm quartz fraction (multi-grain cup) in order to observe the signal components: the sequence, including a first LM-OSL measurement (blue LED at 125°C with power linearly increased from 0 to 100 mW/cm^2 in 1000 s), and cycles of dosing (100 Gy), preheating and LM-OSL measurement was repeated by varying the preheating condition(none, 200°C cut, 220°C 10 s, 260°C 10 s). The same protocol was applied to the Risø calibration quartz, known to be dominated by the fast component (Hansen et al., 2015). We will not comment here on the effect of the different preheating conditions. What must be emphasized is that the Border Cave quartz grains are dominated by the fast component (Fig. 2).

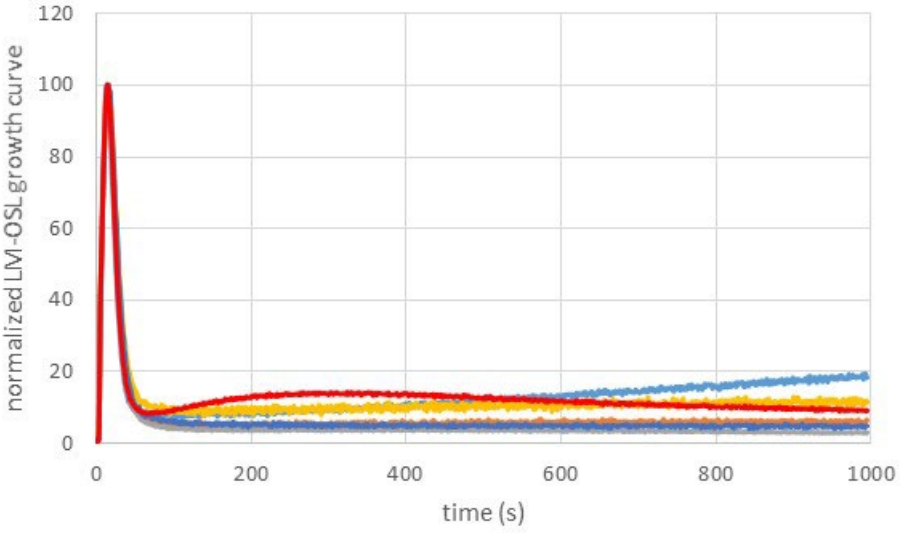

Figure 2 : Normalized LM-OSL glow curves for different BDC samples, after a regenerative dose of 122 Gy and a cut-heat of 200°C. The red curve corresponds to the Risø calibration quartz (batch 123).

To start with, the SAR protocol was tested on sample BDC3. A dose recovery test (DRT) was performed in order to check whether a known laboratory given dose would be accurately determined: the sample was bleached for one minute in a solar simulator (Hönle UVACube 400), left in the dark for over three hours and bleached again at room temperature with blue LEDs in the reader. Then, a known beta dose of 220 Gy was given in the reader and the SAR protocol (Fig. 3) was applied. An additional recycling cycle including an IRSL stimulation at 50°C was performed in order to check for feldspar contamination (Duller, 2003). The data have been analyzed with Analyst v4.57 (Duller, 2015). The growth curves were fitted with single saturated exponentials such as $Lx/Tx = a\,(1-\exp((-D+b)/D_0))$, where a, b and D_0 are the fitting parameters, Lx/Tx is the sensitivity corrected luminescence signal and D is the dose. Grains were rejected if their sensitivity was low (signal <3 times background; relative test dose error >10%), if the recuperation was high (ratio of signals for a 0 Gy dose and the highest regenerative dose >5%), and if the recycling was poor (recycling ratio not consistent with [0.9;1.1]). Grains were also rejected if their natural signal was higher than, or at, the saturation level. Since those grains are numerous (20% of the grains that pass the sensitivity and recuperation criteria for the DRT), an additional criterion based on the D_0 value was applied (Thomsen et al., 2016). It has been shown (see also Li et al., 2017) that when the true mean De is high, such that many grains are rejected because of saturation - i.e. because of low D_0 values - the estimated mean De of the remaining grains is underestimated. Following Thomsen et al. (2016) who suggest plotting De as a function of D_0, one can generally observe the increase of the selected De values as a function of the D_0 values until a plateau is reached. This plateau occurs for the D_0 range values where no more grains are rejected because of saturation.

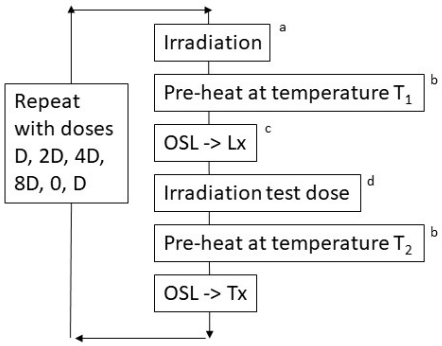

Figure 3. SAR protocol. a) No irradiation was given during the first cycle, where the natural signal is measured. b) T_1 was fixed at 260°C for 10 s; T_2 was 220°C for 10 s; c) The signal is stimulated for 0.8 s. The first 0.05 s and last 0.1 s were taken as signal and back-ground respectively. d) Test dose was 37 Gy.

Figure 4 displays the De/D_0 plot for sample BDC3. This sample has D_0 values well over 200 Gy, up to 800 Gy, which is unusual for quartz grains. The 200-800 Gy range for the D_0 value is suitable for recording De_s in the expected De range of the BDC samples. Moreover, in the plateau zone, the ratio of the central De (central age model, CAM, Galbraith et al., 1999) to the expected dose is consistent with unity at two sigma. This suggests *a priori* that the SAR protocol can be applied successfully at least for this sample, leading to an equivalent dose of 220 Gy. Interestingly enough, it is evident (Fig. sup.3) that the high D_0 grains are not the brightest grains, and inversely the brighter grains do not display D_0 values >300 Gy. While bright grains are typically preferred (e.g. Anechitei-Deacu et al., 2018; Thomsen et al., 2012) we chose to investigate the dimmer – high D_0 grains further.

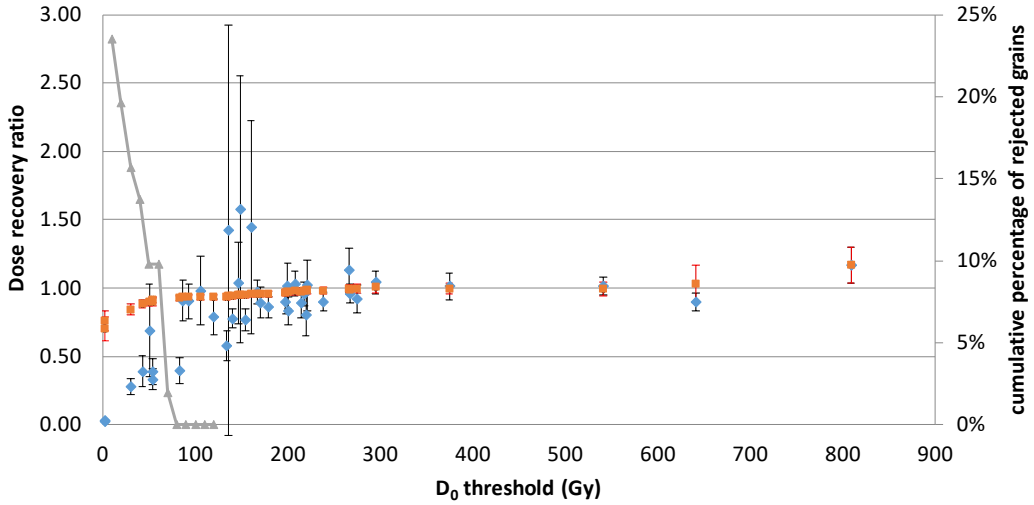

Figure 4. De/D_0 plot for the dose recovery test of BDC3. The dose to recover was about 220 Gy. The blue dots represent the data for the grains that pass the rejection criteria. The orange dots correspond to the central dose (ratio) when only the grains above the corresponding D_0 threshold value are taken into account. The grey curve shows the cumulative percentage of grains that have been rejected because of saturation.

The same protocol was then applied to the natural sample (BDC3). Figure 5 shows that in contrast to the dose recovery test, no clear plateau is reached for the highest D_0 values. On the contrary, unexpectedly low De values are obtained (mean <100 Gy), while the expected De is over 170 Gy. Note that the D_0/sensitivity pattern, however, remains identical (Fig. sup.4). This behavior was observed with other BDC samples as well (data not shown), and the reason for the dose drop was investigated.

In 2000, Yoshida et al. suggested using "supergrains", i.e. grains with high D_0 values (and in their case, bright signals), in order to extend the age range of optical dating. On the other hand, many underestimates of high De_s have been reported in the literature for quartz grains (Peng et al., 2022 and references therein). This underestimate can be due to the presence of low D_0 values, and proper handling of single grain data has been shown in some cases to overcome this issue (Thomsen et al., 2016; Li et al., 2017). However, additional issues have been raised, such as, first, the domination by medium and/or slow components which are thermally unstable (e.g. Jain et al., 2003), fading in quartz of volcanic origin, or in some loess (Bonde et al., 2001; Tsukamoto et al., 2007; Perić et al., 2021), and, secondly, differences in competition for free charges, which can occur during stimulation and/or dosing and/or heating, between the traps and luminescence centers for natural and artificial dose rates (Bailey et al., 2004a). The consequence of this difference in competition is that the regenerative dose response curve is not equivalent to the natural dose response curve, and/or the natural test dose signal is not a good surrogate for the sensitivity of the natural signal (e.g. Singhvi et al., 2011).

Therefore, three hypotheses have been formulated: 1) is this quartz signal unstable? 2) Is there an issue of uncorrected sensitivity change? 3) Is there an issue with the scale of dose rate for natural versus artificial irradiation?

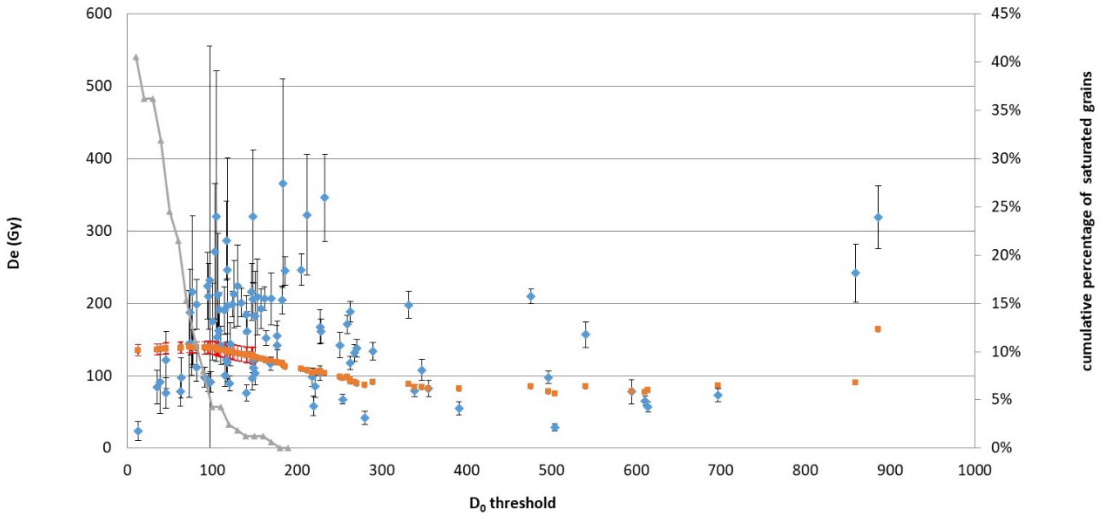

Figure 5. De/D_0 plot for the De measurements of BDC3. The blue dots represent the data for the grains that pass the rejection criteria. The orange dots correspond to the central dose (ratio) when only the grains above the corresponding D_0 threshold value are taken into account. The grey curve shows the cumulative percentage of grains that have been rejected because of saturation.

Hypothesis 1

While thermal instability has been reported for medium and some slow components (e.g. Jain et al., 2003), it is generally not expected for the fast component. To our knowledge, only Steffen et al. (2009) identified fast component instability for one of their samples, while being critical about their calculation of the trap lifetime. Since the BDC samples are dominated by the fast component, this instability is unexpected. However, the LM-OSL tests have been performed at the multigrain scale and the LM-OSL signal is dominated by the brighter grains which are not the high D_0 ones. Consequently, additional inspection of the glow curves was performed at the single grain level. Comparisons were made for CW-OSL glow curves of BDC3 (i.e. glow curves obtained with constant temperature and stimulation power) between those corresponding to D_0 values >300 Gy and those with D_0 values in the [100-200 Gy] interval displaying De_s >180 Gy (Fig. sup.5). No fast ratio such as the one defined by Durcan and Duller (2011) was calculated. Indeed, it requires the knowledge of the stimulation light intensity and photo-ionization cross-section of fast and medium component, which are not known in our measurement conditions and which appear to be variable with single grain stimulation (Duller, 2012). Nonetheless, it is still possible to define an arbitrary ratio comparing the signal at the first channel (first 0.017s) and a later part of the signal (here 0.12-0.15 s) that allows for a partial description of the decay rate and comparison between the two groups. No correlation could be observed between the decay rates of the glow curve and the De values. In other words, the decay rates in the >300Gy D_0 /low De_s group is not slower than in the lower D_0 /higher De_s group (Fig. sup.6). We conclude that medium or slow components are not responsible for the drop of De_s with large D_0 values.

Fading issues (i.e. instability unpredicted by thermodynamics laws) are known to affect feldspar grains (see Section 6.2) and may lead to severe De underestimates if not corrected for. However, SEM-EDS analyses did not detect feldspar inclusions within the quartz grains, and IRSL tests (Duller, 2003)

did not suggest that the high D_0 / low De grains actually correspond to feldspar contaminants. Fading has already been reported for quartz of volcanic origin (Bonde et al., 2001; Tsukamoto et al., 2007) or from loess (e.g. Perić et al., 2021). Consequently, the fading rates for some of our quartz grains were measured. Grains of a disc of sample BDC1 that showed a similar behavior to those of BDC3, were used after the SAR measurements and identification of high D_0 grains. Successive cycles including irradiation (180 Gy), preheat (260 °C 10 s), pause (delay of 0, 1, 10 and 100 hours), and single grain OSL measurements (corrected for sensitivity change) were performed. The sensitivity-corrected signal was then plotted as a function of the delay. The observation of the signal/delay relationship was hampered by the high uncertainty of the signal and the high scatter of the data. Moreover, it was performed on a limited number of grains. However, the mean fading rate of the high D_0 (here >200Gy) grains was found to be consistent with 0, while one would expect for this sample a *g* value (at 2 days) of 12% in order to explain the observed De underestimate in case of a logarithmic decay (Fig. sup.7). Therefore, fading does not seem to be the cause of the low De values for the quartz grains.

Hypothesis 2

It is well known that the SAR protocol allows one to record and correct sensitivity changes that occur from the first (natural) test dose measurement (Murray and Wintle, 2000), but that it cannot guarantee that this first test dose is an appropriate surrogate of the sensitivity of the natural De signal. Singhvi et al. (2011) have shown that sensitivity changes can occur during the measurement of the natural OSL signal. They suggested using the 110°C TL peak measured before and after the natural signal (using an additional small test dose) in order to correct for this issue, for multi-grain measurements (Natural Sensitivity Corrected–SAR procedure). However, unless displaying one grain per cup (Chauhan et al., 2019), which would be far too long to be practical, this is not applicable to standard single grain measurements performed with single grain discs. Another possibility for correcting early sensitivity changes, is to apply a single additive and regenerative dose protocol (SARA, Mejdahl and Bøtter-Jensen, 1994). In this protocol, a known dose is added before the SAR protocol is applied and the recovered dose is plotted as a function of the added dose (hereafter: SARA plot). In cases where all sensitivity changes are properly taken into account (and do not depend on the added dose), the slope of the plot is consistent with unity. However, if a sensitivity change occurs during the natural signal measurement or between the natural (or natural+dose) and the subsequent test dose measurement, the slope is different from unity and the correct De is deduced by extrapolation along the X axis.

The SARA protocol was attempted on sample BDC6. Figure sup.8 displays the De/D_0 plots for each added dose and Figure sup.9 shows the SARA plot obtained for D_0 values between 0 and 300, 300 and 600 and >600 Gy. The De/D_0 plots show that when a dose is added before the SAR measurements, the De plateau appears at high D_0 values. Whatever the D_0 range, the slope of the SARA plot significantly differs from unity, suggesting that there are indeed issues with sensitivity changes. However, the corrected De drops from 332 ± 9 Gy for the 0-300 Gy D_0 range, to 103 ± 3 Gy for D_0 >600 Gy. We conclude that the SARA protocol does not allow us to solve the issue of De underestimate for the high D_0 values.

Hypothesis 3

Based on simulations, Bailey et al. (2004) suggested that the dose rate of the artificial source, which is about 10^9 times higher than the natural dose rate, induces systematic overestimates of the equivalent doses when they are >40 Gy. More recently, Peng et al. (2022), using a slightly different quartz model, showed that the difference between artificial and natural dose rates could, on the contrary, lead to systematic underestimates of the De_s. The over- or underestimates of the De_s are due

to significant differences in competition for free charges of the various traps and recombination centers for low (natural) and high (artificial) dose rates. In order to mimic the natural state of competition, Bailey et al. (2004) suggested applying pulse irradiations: the regenerative doses are split under a series of smaller doses (typically 10 Gy) and a short preheat (240°C cut) is given after each dose. This was attempted on sample BDC3 (Fig. sup.10). The main effect of this pulse irradiation mode seems to be the disappearance of all D_0 values >400 Gy (with the standard irradiation mode, the high D_0 values represent 11% of the non-saturated grains that pass the sensitivity and recuperation criteria), and a clearer separation between grains that reach 200 Gy, and those that stay below 100 Gy. However, it is not clear if this is only a statistical bias due to the low number of measured grains. Meanwhile, the central De in the 150-400 Gy D_0 range (where no rejection for saturation occurs) is even lower for the pulse irradiation group (101 ± 15 Gy) than for the standard irradiation group (140 ± 11 Gy). This suggests that while the pulse irradiation may have an effect on the D_0 values, it does not solve the issue of different competition levels, as initially suggested.

In summary, despite preliminary tests suggesting that quartz grains with high D_0 values could be suitable for estimating the expected high De, only low De_s were obtained for those grains. While we have tested two alternatives to overcome these issues (i.e. SARA protocol and pulse irradiations), neither was found to be fully efficient. The new method recently proposed by Singhvi et al. (2021) to adapt the multi-grain-natural correction factor to single grains could be considered in subsequent work. Additional research should also explore whether the two groups of grains observed in the D_0 versus sensitivity plot are related to two different sources of grains, i.e. the aeolian part and the weathering of the rhyolitic roof.

6.2 Feldspars

For the 63-80 µm feldspar grains, a post-isothermal post-IRSL (pIT) protocol (Lamothe et al., 2020) has been applied (Fig. 6). This protocol, which uses both the IRSL signal at 50°C (IR50) and post-IR50 IRSL signal at 225°C (IR225), allows one to take into account the fading rates of both signals without the need to measure them. It is expected to give more accurate results than the standard IR50 or postIR50 IR225 or IR290 protocols. The pIT protocol is based on the observation that the decrease of the growth curves due to fading can be mimicked in the laboratory by an annealing, i.e. an additional thermal treatment performed between the regenerative dose and the standard preheat in a post-IR-IRSL measurement cycle. In practice, growth curves are built for both the IR50 and IR225 signals for different annealing times at a given temperature (the temperature has been shown not to be an important factor). Ratios of the De_{IR50} and De_{IR225} obtained for these various annealing times are plotted as a function of the De_{IR50}. This enables calculating the De for which this ratio is equal to unity: this one corresponds to the fading corrected De (hereafter pIT De).

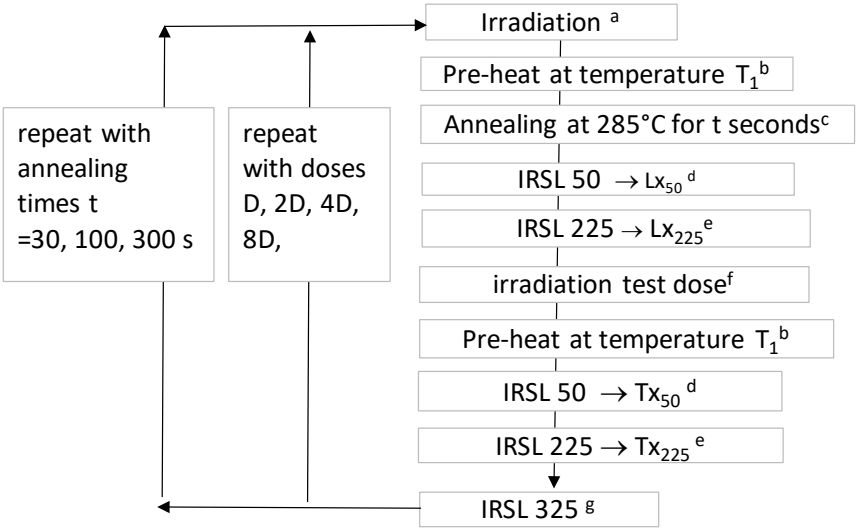

Figure 6. pIT protocol. a) For the very first cycle, no irradiation is given since the natural signal is measured. b) For the first cycle and the first set of regenerative doses, no annealing is given. This corresponds to a standard post-IR50 IRSL225 protocol and is referred to later as annealing "0 s". c) After the dose recovery tests, T_1 was fixed at 265°C for 60 s. d) The IRSL signal was stimulated for 200 s at 50°C. The first 6 s and last 20 s were taken as signal and background respectively. e) The IRSL signal was stimulated for 200 s at 225°C. The first 6 s and last 20 s were taken as signal and background respectively. f) The test dose was fixed at 139 Gy. g) An optical wash was performed with an IRSL stimulation at 325°C for 200 s in order to avoid signal recuperation. Note that all temperature increments were of 2°C/s in order to limit temperature overshoots and ensure better reproducibility of the measurements.

First, the preheat temperatures have been adjusted in order to obtain dose recovery ratios consistent with unity: aliquots of sample BDC4 were bleached for about 1.25 hour in a solar simulator (Höhnle UVACube 400). Then they were given a dose of about 417 Gy and the post-IR50 IR225 protocol was applied (as in Figure 6, without any annealing time), using only one regenerative dose identical to the first dose, following Lamothe et al. (2018). The preheat temperature was increased from 190°C for 60 s to 310°C for 60 s. The residual dose was estimated for a single preheat of 250°C for 60 s, but applied to correct all data. The dose recovery ratios for the IR50 and IR225 signals are shown in Figure 7 (blue dots). The data suggest that a preheat temperature close to 270°C is most suitable. This was further tested on all samples with short dose recovery tests (only one regenerative dose, Figure 7, orange dots), and on some samples (BDC1, 3, 4, 5, 7, 9) with complete (five regenerative doses) dose recovery tests, with a preheat of 265°C for 10 s. The mean dose recovery ratio (Table sup.3) for both the IR50 and IR225 signals are within 5% of unity for the short DRT, and 10% of unity for the complete DRT. The 265°C preheat temperature was applied for the subsequent measurements.

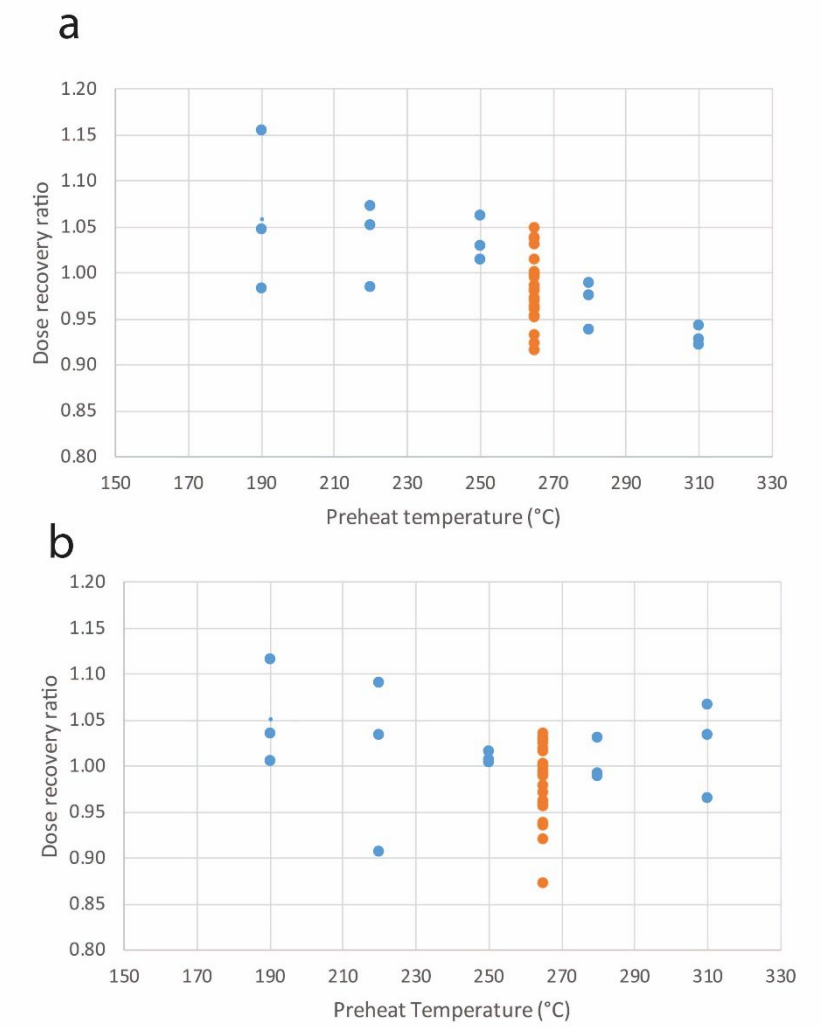

Figure 7. Dose recovery ratio as a function of the preheat temperature a) for the IR50 signal, b) for the IR225 signal. Only one regeneration of 417 Gy dose identical to the dose to recover was given for this test. Blue dots: BDC4, Orange dots: all other samples (3 dots/sample).

Growth curves for an annealing temperature of 285°C and durations of 0, 30 and 100 s were built for 3 to 6 aliquots of each sample. The fit was done with an exponential plus linear saturating exponential. A few growth curves for an annealing time of 300 s were also built, but were found to be unnecessary in the post-processing of the pIT De calculation, so they will not be considered here. Since the measurement time for building one full set of growth curves for one aliquot and getting one pIT De is long (from 24 to 48 hours), it could be advantageous to apply a global growth curve (GGC) approach (e.g. Roberts and Duller, 2004; Li et al., 2015): a mean growth curve can be deduced from the full measurements of a first set of aliquots. Then, only the natural-sensitivity corrected signals (Ln/Tn) are measured on other aliquots and projected on the GGC.

The growth curves obtained on the different aliquots and samples have thus been compared in order to decide whether a GGC approach could be successfully applied or not. All Lx/Tx data have been gathered in figures 8a to 8f (one figure for each signal –IR50 or IR225-, and each annealing time, -0, 30, 100 s-). The scatter increases with increasing annealing time and with increasing regenerative dose, but stands overall between 2 and 13% for all aliquots of all gathered samples. The GGC was then calculated for each annealing time and each IR signal. The pIT De based on the individual growth curves

and on the GGC have been compared (Table 4). Their ratio is within 10% of unity for aliquots of BDC1, 3, 4, 5, 6, 9, but not for BDC2, 7, 8, 10. While BDC7 and BDC8, which are much older, are likely more sensitive to small changes in the growth curves, it is not the case for BDC2 and 10. On the other hand we do not have evidence that these samples have different mineralogical compositions, which would imply a different behavior. Consequently, the GGC approach has been applied to all samples. Only the global consistency of the results suggests *a posteriori* that this approach is relevant for all samples.

Table 4. Comparison of De_s obtained with the individual growth curve approach (each aliquot is submitted to the full measurement protocol as shown in Figure 6), and with the GGC approach (the Ln/Tn values for each aliquot are projected on the mean growth curves calculated from all individual growth curves).

BDC	global growth curves		individual growth curves		ratio GGC/individual De	
1	202	± 1	212	± 13	0.95	± 0.06
1	255	± 1				
1	216	± 1	227	± 2	0.95	± 0.01
2	276	± 2	376	± 4	0.73	± 0.01
2	253	± 2	295	± 3	0.86	± 0.01
2	260	± 1	277	± 1	0.94	± 0.01
2	239	± 1	273	± 4	0.88	± 0.01
3	266	± 1	269	± 9	0.99	± 0.03
3	344	± 2	375	± 10	0.92	± 0.02
3	257	± 1	269	± 2	0.96	± 0.01
4	311	± 2	324	± 2	0.96	± 0.01
4	389	± 2	356	± 4	1.09	± 0.01
4	301	± 1	320	± 2	0.94	± 0.01
5	407	± 3	398	± 6	1.02	± 0.02
5	366	± 2	367	± 4	1.00	± 0.01
5	335	± 2	316	± 2	1.06	± 0.01
6	304	± 2	321	± 2	0.95	± 0.01
6	345	± 2	334	± 1	1.03	± 0.01
6	310	± 2	308	± 1	1.01	± 0.01
7	1386	± 31	1458	± 20	0.95	± 0.02
7	1886	± 14	980	± 26	1.92	± 0.05
7	766	± 9	914	± 65	0.84	± 0.06
8	978	± 17	717	± 7	1.36	± 0.03
8	1250	± 28	1106	± 26	1.13	± 0.04
8	1655	± 24	889	± 10	1.86	± 0.03
9	418	± 6				
9	382	± 3	369	± 4	1.03	± 0.01
9	289	± 1	289	± 13	1.00	± 0.05
10	344	± 2				
10	230	± 1				
10	389	± 2	596	± 125	0.65	± 0.14
10	262	± 1	392	± 22	0.67	± 0.04
10	468	± 15	345	± 3	1.36	± 0.04
10	185	± 1	183	± 1	1.02	± 0.01

Consequently, about 20 additional aliquots were measured for each sample in order to obtain Ln/Tn ratios. These were projected on the GGC and the corresponding De_{IR50} and De_{IR225} were calculated. Figure 9 displays three examples giving the ratio of the De_{IR50} and De_{IR225} as a function of De_{IR50} for each annealing time, which allows us to calculate the pIT De. In the inset of Figure 9, the ratio of the De_{IR50} and De_{IR225} is plotted as a function of the annealing time, allowing us to calculate the annealing time corresponding to the pIT De. Figure 10 displays the pIT De_s versus annealing times for each sample. For all samples in Figure 10, it can be observed that the pIT De_s slightly increase with the annealing times while they are expected to be independent. In order to understand this apparent correlation, we must observe the isodose plot (Fig. 11), where the mean Lx/Tx values for IR225 signals are plotted as a function of mean Lx/Tx values for IR50 signals for each annealing time and regenerative dose. The Ln/Tn values of each sample are also reported on this isodose plot. Lamothe et al. (2020, their Fig. 2) have indeed shown that each Lx/Tx (or Ln/Tn) couple corresponds to a single couple of pIT De and

annealing time. Moreover, it can be deduced from this isodose plot that, if the IR225 signal had not been properly bleached in the past, the position of the corresponding Ln/Tn point would be higher than it should be. Consequently, it would appear as corresponding to a higher dose, with an apparent higher annealing time. Considering our data plotted in Figure 11, we interpret the dependency of the pIT De and annealing time as evidence for incomplete bleaching, at least for the IR225 signal which is known to be less bleachable than the IR50 signal. This incomplete bleaching is unexpected if we consider the aeolian component of the sediments and the slow sedimentation rates. However, part of the grains also come from rhyolite fragments that fall off the roof and may have disintegrated while already buried; hence, some grains might have not fully bleached.

Based on this interpretation, it can be concluded that the mean pIT De (Table 5) for each sample likely overestimates the targeted De. Attempts have been made to apply the Minimum Age Model (MAM, Galbraith et al., 1999), but results are extremely sensitive to the supposed over-dispersion of the well bleached distribution, and we lack this information. On the other hand, if the lowest pIT De_s of each distribution correspond to well-bleached grains, then the extrapolated pIT De at 0 s annealing should be consistent or lower than the targeted mean pIT De (Table 5). However, we cannot exclude that none of the grains was actually fully bleached at time of deposition. Therefore, we will keep two De estimates for each sample: the mean pIT De that we consider as a maximum De (it overestimates the targeted De), and the 0 s annealing-extrapolated De estimate that we consider as a minimum De estimate, in the case where some of the aliquots contain only grains that were fully bleached at deposition. We expect the targeted age to be closer to (or consistent with) the minimum rather than the maximum pIT age estimate.

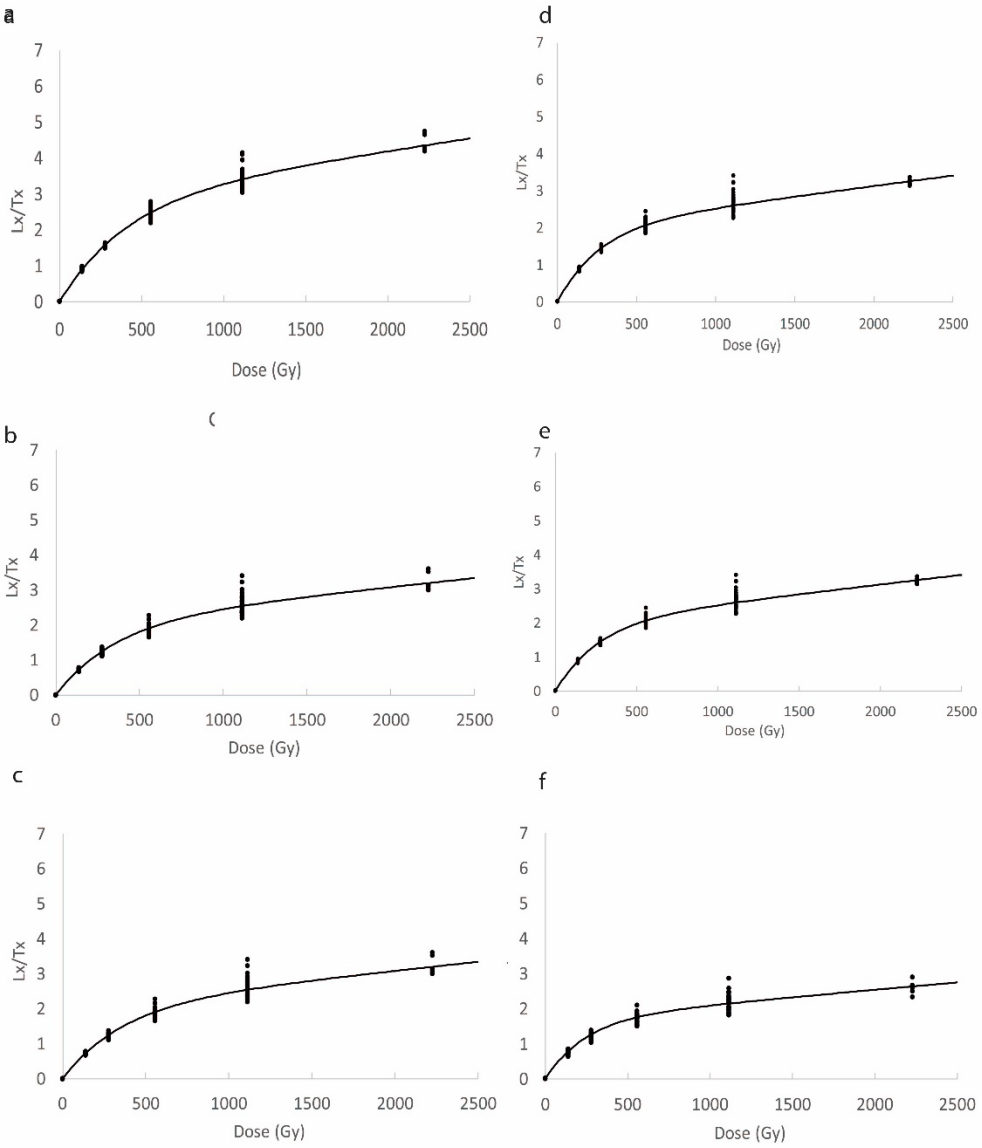

562

563 *Figure 8. Global growth curves calculated for all BDC samples (3 to 6 aliquots per samples). a: IR50, annealing 0 s; b: IR50*
564 *annealing 10 s; c: IR50 annealing 30 s; d: IR225 annealing 0 s; e: IR225 annealing 30 s; f: IR225 annealing 100 s. The Ln/Tn*
565 *signal of each aliquot can be projected onto each of these GGCs and the corresponding De is calculated by interpolation.*

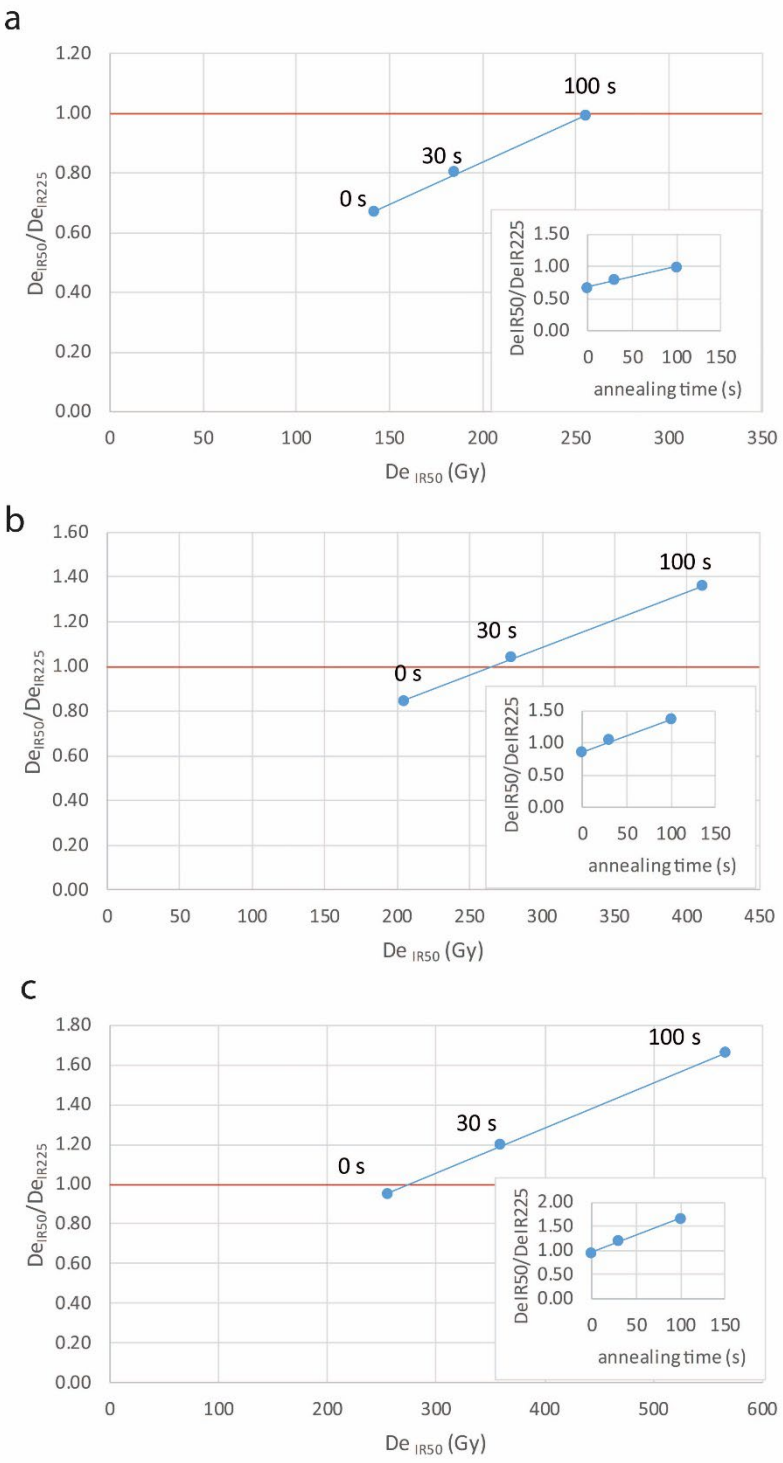

Figure 9. Ratio of De_s for IR50 and IR225 signals for three different aliquots of BDC3 as a function of De_{IR50} (GGC approach). The interpolation allows one to calculate the fading corrected De (pIT De), i.e. the De for which the ratio is unity. In the inset the ratio is plotted as a function of the annealing times. The annealing time corresponding to a ratio equal to one can also be deduced by interpolation.

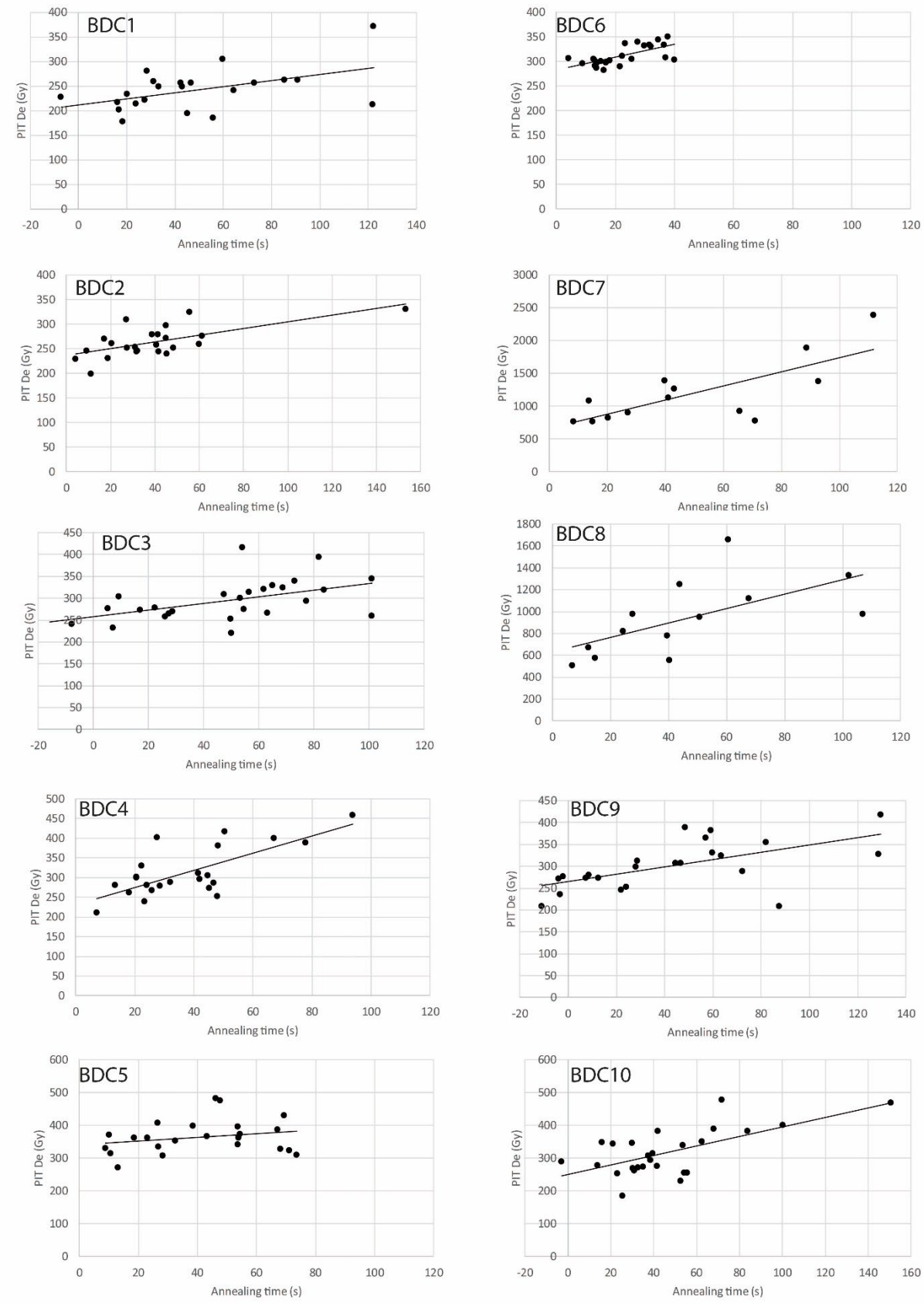

Figure 10. pIT De$_s$ as a function of annealing times for each sediment sample. Linear regression curves highlight the fact that despite the scatter, in each sample the pIT De tends to increase with the annealing time. Error bars are smaller than the points.

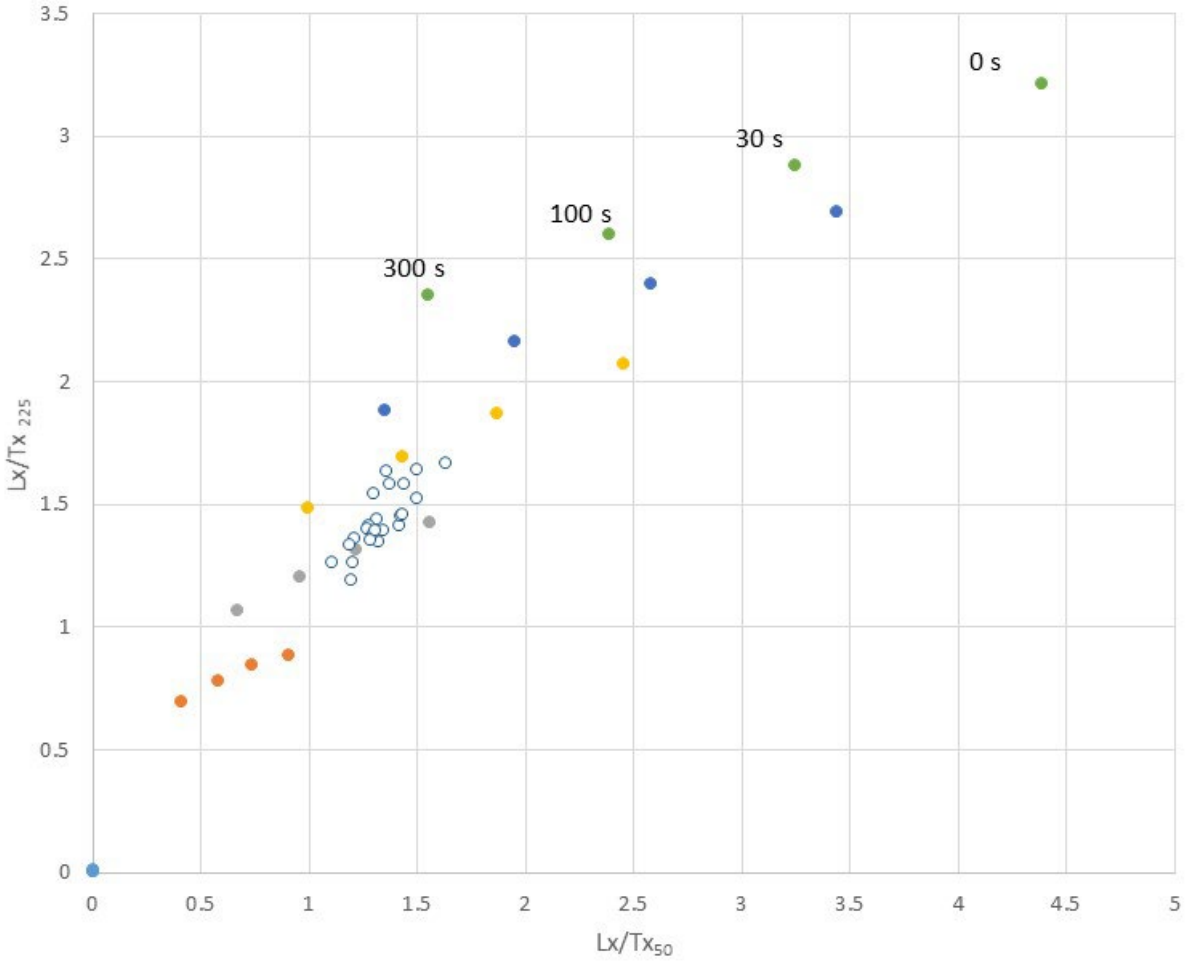

Figure 11. Isodose plot. The mean Lx/Tx_{225} for each regenerative dose and annealing time of the GGC are plotted as a function of the mean Lx/Tx_{50}. The annealing times are indicated on the plot. Light blue dots: 0 Gy; orange dots: 139 Gy; grey dots: 278 Gy; yellow dots: 556 Gy; dark blue dots: 1113 Gy; green dots: 2227 Gy. White dots: Ln/Tn values for BDC4. This isodose plot constitutes a chart in a "fading corrected space", where the pIT De and corresponding annealing time for each Ln/Tn couple can be immediately deduced. However, in case of poor bleaching, Lx/Tx_{225} (and to a lesser extent Lx/Tx_{50}) will be higher than it should be. Consequently, the corresponding point will appear on a higher isodose curve and will correspond to an apparently higher annealing time. In other words, the poorer the bleaching, the higher the apparent pIT De and the higher the apparent annealing time.

Table 5. pIT De estimates for the 63-80 µm feldspar grains of the Border Cave samples. Two estimates are presented: the mean pIT De which overestimates the targeted De because of poor bleaching, considered as a maximum De estimate; the 0 s-annealing extrapolated pIT De which underestimates or is close to the targeted De.

Sample	0 s annealing-extrapolated pIT De (Gy)		mean pIT De (Gy)	
BDC 1	212	± 15	241	± 9
BDC 2	236	± 9	264	± 6
BDC 3	257	± 16	295	± 9
BDC 4	231	± 20	313	± 13
BDC 5	341	± 23	364	± 11
BDC 6	282	± 8	312	± 4
BDC 7	660	± 169	1190	± 135
BDC 8	630	± 139	935	± 94
BDC 9	265	± 14	301	± 12
BDC 10	250	± 20	317	± 14

7. Ages and discussion

The minimum and maximum pIT ages are plotted in Figure 12 and given in Table 6. In Figure 12, we have also plotted the ESR age estimates (Grün et al., 2003), and the results of three different hierarchical Bayesian models. We will first discuss the Bayesian models, then compare the pIT ages with the Bayesian models, and finally discuss the archaeological and sedimentological implications.

As is commonly known, Bayes theorem allows one to combine chronological probabilistic information (e.g. radiometric or luminescence measurements) with probabilistic *a priori* information (e.g., stratigraphic ordering of archaeological and/or sedimentary levels) obtained from an archaeological site. When Bayesian age modeling methods are applied to an archaeological context, the age measurements (e.g., radiocarbon (^{14}C), OSL, ESR) and the *a priori* information lead to *a posteriori* results that improve our understanding of the timing and duration of archaeological events.

Bayesian models based on ^{14}C dates and *a priori* chronostratigraphic information have become very common during recent decades. In cases where ESR and OSL data are included in a Bayesian model, additional issues must be considered because such ages (when obtained for a given stratigraphic sequence) are not fully independent since they potentially share parameters (e.g. cosmic or gamma dose rate) and systematic uncertainties (Rhodes et al., 2003). Not taking this special feature into account can lead to an underestimation of the uncertainties associated with the *a posteriori* results. While specific methods have been developed (e.g. Philippe et al., 2019), Millard (2006) was the first to propose a relevant Bayesian method integrating a hierarchical approach adapted to ESR ages, which he applied to the Border Cave ESR data. His calculations were run on the ESR data available for each subsample (two or three per tooth), corrected for the cosmic dose rate (following Grün et al., 2003), using WinBUGS, and assuming continuous deposition without any hiatuses. The results for each tooth are presented only graphically in the 2006 paper, but the 95% Highest Posterior Density (HPD) for the boundaries have been kindly provided by A. Millard (pers. comm) and are reported in Table sup.4 and Figure 12.

In addition to Millard's analyses, we produced two hierarchical Bayesian age models using the ChronoModel software package (Lanos and Dufresne, 2019; Lanos and Philippe, 2018), and the reasons for this choice are detailed in the Supplementary Information in Section 5. The advantage of ChronoModel is that the Event concept, on which it is based, avoids the compression effect that occurs

in packages that employ the Naylor-Smith-Buck-Christen (NSBC) prior (which is used in software packages such as BCal or OxCal; Bronk-Ramsey, 2001; Buck et al., 1999; Lanos and Philippe, 2018). In addition, ChronoModel's hierarchical model automatically penalizes outliers, so there is no need to reject data before running the model or to run multiple generations of a model, for early generations are used to identify outliers, which are removed before running a subsequent model. Our models employed all available radiocarbon and ESR data (also corrected for the cosmic dose rate) and assumed continuous deposition without any hiatuses. Two models were run: one in which each subsample is taken into account, and all the subsamples of a tooth, together, constitute an Event; and a second one in which an average ESR age for each tooth constitutes an Event.

The two models we produced with ChronoModel compare well with the one produced by Millard (Table sup.5, Fig. 12), despite differing mathematical foundations. The small shift for the boundaries of 1 WA/1 BS and 2 BS/1 WA is likely due to the fact that Millard did not incorporate the then available ^{14}C ages. This observation shows that, although Millard's model takes into account more finely the dependence between samples and the systematic uncertainties they share, the results of our Bayesian models are primarily governed by the *a priori* information, such as stratigraphic relationships, since the Event date concept is the central element of our models.

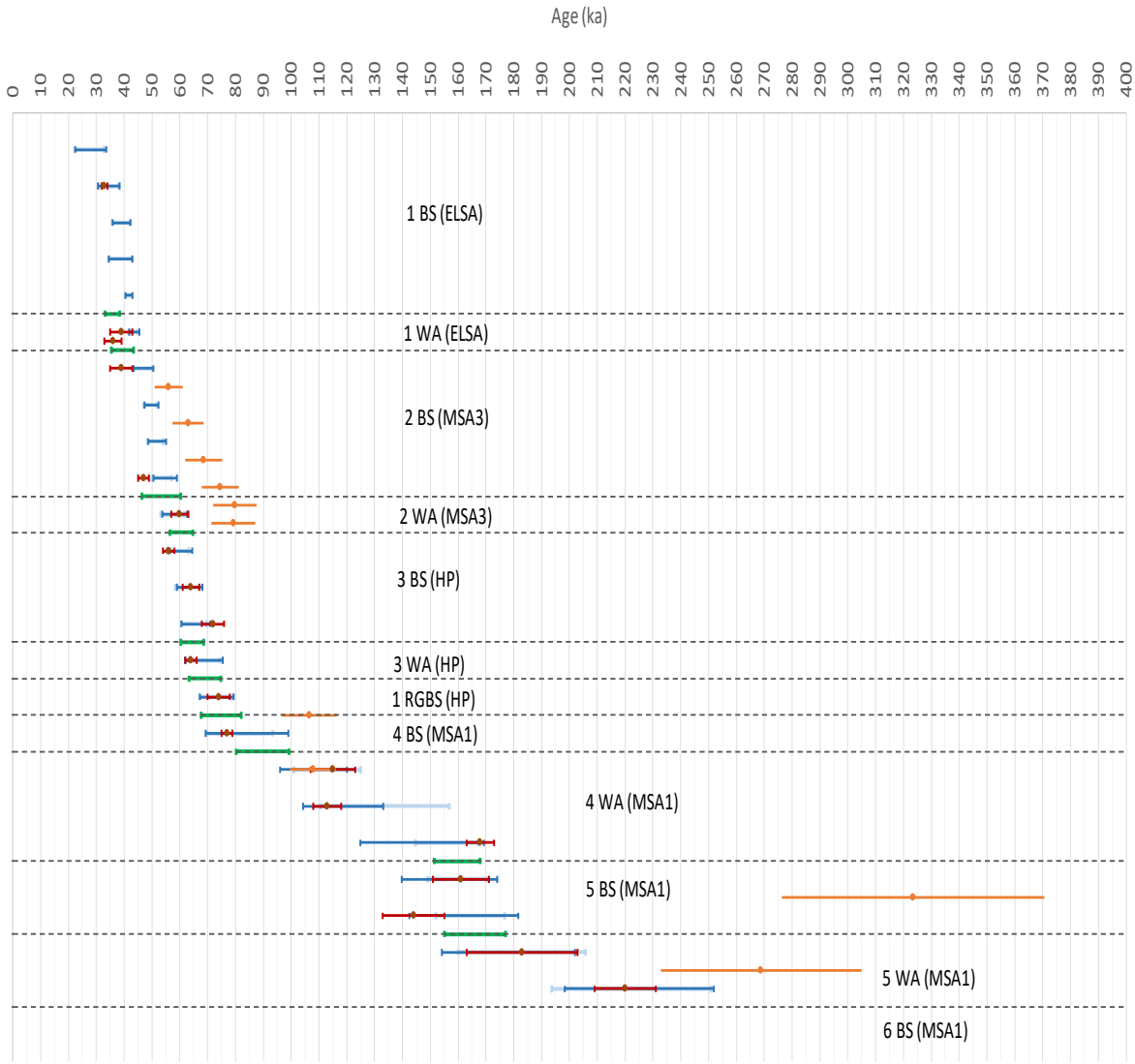
Age (ka)
0
10
20
30
40
50
60
70
80
90
100
110
120
130
140
150
160
170
180
190
200
210
220
230
240
250
260
270
280
290
300
310
320
330
340
350
360
370
380
390
400
1 BS (ELSA)
1 WA (ELSA)
2 BS (MSA3)
2 WA (MSA3)
3 BS (HP)
3 WA (HP)
1 RGBS (HP)
4 BS (MSA1)
4 WA (MSA1)
5 BS (MSA1)
5 WA (MSA1)
6 BS (MSA1)

637

638

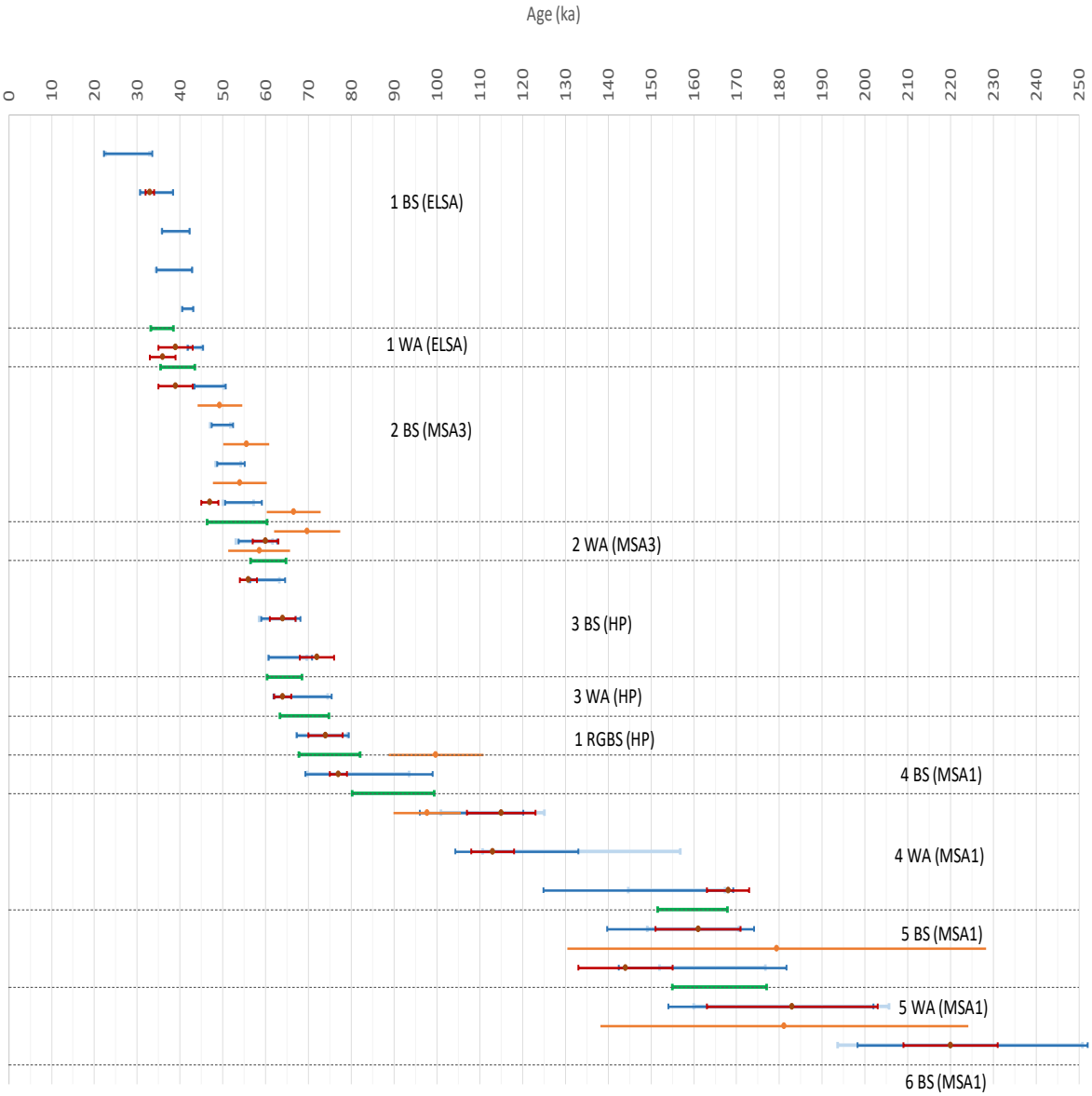

Figure 12. Synthesis of ages for the Border Cave stratigraphic sequence. Red dots: ESR ages from Grün et al. (2003; mean for each layer). Dark blue and light blue bars: Bayesian models based on ESR and radiocarbon data. Dark blue: from ages for each tooth subsample; Light blue: from the average ESR ages for each tooth. Green bars: Bayesian models for transition between members based on the ESR ages, after Millard (2006). Orange dots: ages from feldspar grains obtained with the pIT protocol. Top figure: mean pIT age estimates. Bottom figure: minimum pIT age estimates. ESR and pIT ages are given at 1 σ, while Bayesian results present the 95% HPD.

Table 6. Ages based on the pIT protocol applied to 63-80 µm feldspar grains. The samples are ordered following the same stratigraphic order as in Figure 12. The relative stratigraphic correlations between BDC1 and 2 as well as BDC9 and 10 are speculative.

sample	member	excavation area	layer	cultural attribution	minimum age (ka)		maximum age (ka)	
BDC 1	2 BS	northern	Grass Mat Camilla	MSA 3	49	± 5	56	± 5
BDC 9	2 BS	southern	Brown Caby	MSA 3	55	± 5	63	± 6
BDC 2	2 BS	northern	Yellowish Brown Caz	MSA 3	67	± 6	75	± 7
BDC 10	2 BS	southern	Brown Caby	MSA 3	54	± 6	69	± 7
BDC 3	2 WA lower	northern	Dossy unit above combustion feature 3	MSA 3	70	± 8	80	± 8
BDC 4	2 WA lower	northern	Dossy unit above combustion feature 3	MSA 3	58	± 7	79	± 8
BDC 5	1 RGBS/4 BS	northern	Very Dark Brown Faan	HP/MSA 1	100	± 11	106	± 10
BDC 6	4 WA	northern	White Idaho	MSA 1	98	± 8	108	± 8
BDC 7	5 BS	northern	Brown John	MSA 1	179	± 49	324	± 47
BDC 8	5 WA	northern	Dark Brown Kevin	MSA 1	181	± 43	269	± 36

In Figure 12, elevations relative to datum point for individual samples are not reported because such information is lacking for the ESR samples and also because of the slope of the deposits (deposits have a pronounced gradient and so single units have a wide range of elevations, i.e. an elevation cannot be correlated directly to a whole unit). Moreover, within a member, the relative stratigraphic relationship between the ESR samples from Peter Beaumont's excavations and the pIT samples from the current excavation, cannot be determined with precision. Within a member, only the relative relationship between the ESR samples, on the one hand, and between the pIT samples, on the other, are meaningful. In addition, BDC1, 2 and BDC9, 10, are all attributed to 2 BS but come from different exposed excavation sections and it is not clear yet how the 2 BS subunits in the northern stratigraphy correlate with the southern 2 BS excavation. So, their relative stratigraphic positioning within each member in Figure 12 is not indicative of their relative intra-member stratigraphic relationship.

While the maximum pIT age estimates are significantly higher than the ESR age estimates and their Bayesian models, the minimum pIT age estimates are consistent with these ones, in particular for the top samples (the error estimates for BDC7 and 8 in Members 5 BS and 5 WA are unfortunately very large, so not very informative). Therefore, if our assumption that the targeted ages are close to the minimum pIT age estimates is correct, these results suggest both that the ESR–based chronology and its derived Bayesian models do not have to be challenged and that general attribution of the new excavation to the macro-scale stratigraphic framework of Beaumont is currently acceptable. Improving intra-member stratigraphic resolution will provide significant benefits in tracing changes that fall within error margins of dating methods, and be useful targets for future chronological research.

Border Cave has long been known to be one of the rare sites, along with Diepkloof Rock Shelter (Tribolo et al., 2013), where ages older than 65 ka have been obtained for the Howiesons Poort levels. Jacobs et al. (2008) have argued that the pattern observed at Border Cave was probably only a statistical issue (due to the large uncertainties) and that the ESR data from Border Cave were actually consistent at two sigma with their estimate of 65 ± 3 ka (95% CI) for the start of the Howiesons Poort (revised to 62-71 ka in Jacobs and Roberts, 2017). The new data do not invalidate the >65 ka ages for the members that have been attributed to the Howiesons Poort by Beaumont (e.g. Grün and Beaumont, 2001). Sample BDC5, in particular, at the base of the members attributed to the Howiesons Poort is too imprecise both spatially and temporally. Further sampling in 3 BS, 3 WA and 1 RGBS would be helpful for further clarification. However, most importantly, new technological analyses of the concerned members suggest that the Howiesons Poort cultural attribution as a whole needs to be taken with caution. In his Master's thesis, Beaumont (1978) attributed 3 BS, 3 WA and 1 RGBS to "Epi-Pietersburg of the old-second intermediate", renamed Howiesons Poort in Grün and Beaumont (1990).

This was based on the presence of blades, backed elements and *'Châtelperron or Abri Audi* knives' and sometimes small, pressure-flaked arrowheads. We found very few of them in our new excavation (e.g. only one *Châtelperron* backed piece in Member 1 RGBS layer Ea and one backed piece in 1 RGBS layer Easy). However, in the upper Members 2 WA and 2 BS, Beaumont also mentioned trapeze backed pieces, which he drew as some of the most characteristic items of the MSA 3/post-Howiesons Poort at Border Cave. Hence, at Border Cave, as with other MSA sites in South Africa (e.g. Sibudu Cave) where they also appear in pre-Still Bay, Still Bay, and post-Howiesons Poort layers, isolated backed pieces cannot be used as an unequivocal marker for the Howiesons Poort.

The current chronological data do not necessarily clarify our understanding of hiatuses or erosional phases observed in the stratigraphy (Stratford et al., 2022). For example, the current temporal resolution is not sufficient to highlight several sedimentological sub-units with disconformities that appear in Members 2 WA and 5 BS (Stratford et al., 2022), including a technological change within Member 2 WA (de la Peña et al., in press). Layer Brown Caby, in Member 2 BS, dated with BDC9 and 10 has a low frequency of artefacts, but its age is indistinguishable from the ages for the relatively artefact rich underlying Member 2 WA. A truncation is also observed between Members 5 BS and 5 WA (Stratford et al., 2022) but it is not obvious in the chronological data. The current uncertainties are too large to identify these sedimentological breaks, and/or the sampling was not sufficient in scope to constrain them adequately. This limitation is not unique to Border Cave and is common in many archaeological sequences. Increasing dating sampling frequency in response to increased stratigraphic resolution, however, may not meaningfully provide additional chronological resolution due to inherent uncertainties. Refinement of the age model will be possible when hiatuses are identified and added to ChronoModel and when additional site formation and material culture data are obtained.

On the other hand, apparent chronological gaps, which were already highlighted by Grün and Beaumont (2001) warrant further investigation. This concerns in particular the transition between 4 BS and 4 WA with only one sample (BDC6) at 100 ka filling a gap between ca. 85 ka and 120 ka, the middle of 4 WA with the lack of chronological data between approximately 120 and 150 ka (remarkably 4 WA represents the member covering the longest interval of time, nearly 70 ka, displaying numerous sub-units), and the base of 5 WA, with the ESR age (and potentially pIT age, though again the uncertainty is too large) at 174 ± 9 ka and the last one at 227 ± 11 ka. We need to clarify whether these apparent gaps are due to a lack of sampling, a halt in sedimentation and archaeological record, or erosion. The base of the sequence (Member 6 BS) should also be sampled for future dating in order to document the deposition of geogenic and anthropogenic sediments in the empty shelter.

Meanwhile, the implications of the ages obtained in this study for our understanding of the Middle Stone Age in southern Africa are significant, and some will only be appreciated with further excavations at the site and at other sites in the region. Despite their consistency and good agreement with the chronology of the upper layers established through numerous ^{14}C ages, the ages obtained in the past for the lower layers of Border Cave have been viewed with some degree of caution due to the implementation of a single dating method, a preliminary and shifting attribution of lithic industries to the techno-complexes in favour at the time of excavation, and the lack of other regional reference sequences covering a time span as extensive as that covered by this site. The ages obtained in our study definitely anchor the archaeological layers of this long sequence in a chronological framework that can be considered as established, even if not perfect. In the future, when the abundant lithic industries present in the sequence (de la Peña et al., in press) have been characterized and coupled with a refinement of the archaeological layers and their mode of formation (Stratford et al., 2022), our present chronological framework will undoubtedly reverberate with other sequences in the region and sub-continent.

8. Conclusion

Following the recent excavations at Border Cave (Backwell et al., this volume), we have re-evaluated the site's chronology via the application of TL to burnt lithics, OSL to quartz grains and IRSL (pIT protocol) to feldspar grains. Both TL and OSL failed for the samples that we tested. The current pIT data, while perfectible, confirm the ESR chronology and validate the tentative identification and attribution of the member boundaries recognized by Backwell and colleagues following Beaumont's member framework. Additional sampling can be refined on that basis in order to explore hiatuses and sedimentation rates. However, poor bleaching might still affect the results. Further methodological improvements will: 1) attempt to work on smaller aliquots, up to single grain aliquots in order to try to isolate fully bleached grains; and 2) correct for the poor bleaching via the new approach proposed by Lamothe et al. (2021). Moreover, while we have measured only Ln and Tn signals, an additional regenerative dose could be measured in order to apply the regeneration normalization method (re-normalization, Li et al., 2015), which has the advantage of reducing the scatter between the growth curves. These improvements, together with additional sampling, will help to further clarifying Border Cave's chronology.

Acknowledgements

This research was funded by a National Geographic Explorer grant (NGS-54810R-19) and DSI-NRF Centre of Excellence in Palaeosciences (Genus) grant (CEOOP2020-1) to Lucinda Backwell. Francesco d'Errico's work is supported by the Research Council of Norway through its Centres of Excellence funding scheme, SFF Centre for Early Sapiens Behaviour (SapienCE), project number 262618, the LaScArBx research programme (ANR-10-LABX-52), and the Talents Programme [grant number: 191022_001]. Work by CT, NM, NB, FD, NC, WEB and FdE was supported by the Grand Programme de Recherche 'Human Past' of the Initiative d'Excellence (IdEx) of Bordeaux University. We are grateful to Amafa for issuing us with an excavation permit (SAH 15/7645). Special thanks to Michel Lamothe for his help and advice concerning the pIT protocol. Thank you also to Andrew Millard for providing the numerical values for the age boundaries of the various members.

References

Anechitei-Deacu, V., Timar-Gabor, A., Thomsen, K.J., Buylaert, J.P., Jain, M., Bailey, M., Murray, A.S., 2018. Single and multi-grain OSL investigations in the high dose range using coarse quartz. Radiat. Meas. 120, 124-130.

778 Backwell, L., Wadley, L., d'Errico, F., Banks, W.E., de la Peña, P., Sievers, C., Stratford, D., Lennox, S.,
779 Wojcieszak, M., Bordy, E., Bradfield, J., 2018. New excavations at Border Cave, KwaZulu-Natal,
780 South Africa. J. Field Archaeol. 43(6), 417-436.
781 Backwell, L., Wadley, L., d'Errico, F., Banks, W., de la Peña, P., Stratford, D., Sievers, C., Laue, G., Vilane,
782 B., Clark, J., Tribolo, C., Beaudet, A., Mauran, G., 2022. Border Cave: A 227,000-year-old archive
783 from the southern African interior. Quaternary Sci. Rev. 291: 107597.
784 Bailey, R.M., 2004. Paper I-simulation of dose absorption in quartz over geological timescales and its
785 implications for the precision and accuracy of optical dating. Radiat. Meas. 38(3), 299-310.
786 Beaumont, P. B., 1978. Border Cave. M.A. dissertation, University of Cape Town. South Africa.
787 Beaumont, P.B., 1980. On the age of Border cave hominids 1-5. Palaeontol. Afr. 23, 21-33.
788 Beaumont, P.B., de Villiers, H., Vogel, J.C., 1978. Modern man in sub-saharan Africa prior to 49000 BP:
789 a review and evaluation with particular reference to Border Cave. S. Afr. J. Sci. 74, 409-419.
790 Beaumont, P.B., Vogel, J.C., 1972. On a new radiocarbon chronology for Africa south of the Equator:
791 part 2. Afr. Stud. 31(3), 155-182.
792 Beaumont, P.B., Miller, G.H., Vogel, J.C., 1992. Contemplating old clues to the impact of the future
793 greenhouse climates in South Africa. S. Afr. J. Sci. 88, 490-498.
794 Bird, M.I., Fifield, L.K., Santos, G.M., Beaumont, P.B., Zhou, Y., Di Tada, M.L., Hausladen, P.A., 2003.
795 Radiocarbon dating from 40-60 ka BP at Border Cave, South Africa. Quaternary Sci. Rev. 22, 943-
796 947.
797 Bonde, A., Murray, A., Friedrich, W.L., 2001. Santorini: luminescence dating of a volcanic province using
798 quartz? Quaternary Sci. Rev. 20(5-9), 789-793.
799 Bøtter-Jensen, L., Bulur, E., Duller, G.A.T., Murray, A.S., 2000. Advances in luminescence instrument
800 systems. Radiat. Meas. 32, 523-528.
801 Brennan, B.J., Lyons, R.G., Phillips, S.W., 1991. Attenuation of alpha particle track dose for spherical
802 grains. Nucl. Tracks Rad. Meas. 18, 249-253.
803 Bronk Ramsey, C., 2001. Development of the radiocarbon calibration program OxCal. Radiocarbon 43,
804 355-363.
805 Buck, C., Christen, J., and James, G., 1999. BCal: an on-line Bayesian radiocarbon calibration tool.
806 Internet Archaeol. 7.
807 Chauhan, N., Singhvi, A.K., 2019. Changes in the optically stimulated luminescence (OSL) sensitivity of
808 single grains of quartz during the measurement of natural OSL: Implications for the reliability of
809 optical ages. Quat. Geochronol. 53, 101004.
810 Cooke. H.B.S. 1941. Unpublished reports presently housed at the National Archives and Records
811 Service (NARS) in Tswane (formerly Pretoria), South Africa
812 (http://www.national.archives.gov.za/), where they are kept in Archaeological Survey Files
813 (source ASW, volume 60, reference 20/1/A and B20/1/2A).
814 d'Errico, F., Backwell, L., Villa, P., Degano, I., Lucejko, J.J., Bamford, M.K., Higham, T., Colombini, M.P.,
815 Beaumont, P.B., 2012. Early evidence of San material culture represented by organic artifacts
816 from Border Cave, South Africa. P. Natl. Acad. Sci. USA. 109(33), 13214-13219.
817 de la Peña, P., Colino, F., d'Errico, F., Wadley, L., Banks, W., Stratford, D., Backwell, L., in press. Lithic
818 technological and spatial analysis of the final Pleistocene at Border Cave, South Africa.
819 Quaternary Sci. Rev.
820 Duller, G.A.T., 2003. Distinguishing quartz and feldspar in single grain luminescence measurements.
821 Radiat. Meas. 37, 161-165.
822 Duller, G.A.T., 2015. The Analyst software package for luminescence data: overview and recent
823 improvements. Ancient TL 33, 35-42.
824 Duller, G.A.T., 2012. Improving the accuracy and precision of equivalent doses determined using the
825 optically stimulated luminescence signal from single grains of quartz. Radiat. Meas. 47(9), 770-
826 777.
827 Durcan, J.A., Duller, G.A.T., 2011. The fast ratio: a rapid measure for testing the dominance of the fast
828 component in the initial OSL signal from quartz. Radiat. Meas. 46(10), 1065-1072.

Galbraith, R.F., Roberts, R.G., Laslett, G.M., Yoshida, H., Olley, J.M., 1999. Optical dating of single and multiple grains of quartz from Jinmium rock shelter, northern Australia: Part I, experimental design and statistical models. Archaeometry 41(2), 339-364.

Grün, R., Beaumont, P.B., 2001. Border Cave revisited: a revised ESR chronology. J. Hum. Evol. 40, 467-482.

Grün, R., Beaumont, P.B., Stringer, C.B., 1990. Electron Spin Resonance ESR dating evidence for early modern humans at Border Cave in South Africa. Nature 344 (6266), 537-539.

Grün, R., Beaumont, P., Tobias, P.V., Eggins, S., 2003. On the age of Border Cave 5 human mandible. J. Hum. Evol. 45, 155-167.

Guérin, G., Mercier, N., Adamiec, G., 2011. Dose rate conversion factors: update. Ancient TL 29, 5-8.

Guérin, G., Mercier, N., Nathan, R., Adamiec, G., Lefrais, Y., 2012. On the use of the infinite matrix assumption and associated concepts: A critical review. Radiat. Meas. 47, 778-85.

Hansen, V., Murray, A., Buylaert, J.P., Yeo, E.Y., Thomsen, K., 2015. A new irradiated quartz for beta source calibration. Radiat. Meas. 81, 123-127.

Huntley, D.J., Baril, M.R., 1997. The K content of the K-feldspars being measured in optical dating or in thermoluminescence dating. Ancient TL 15(1), 11-13.

Huntley, D.J., Hancock, R.G.V., 2001. The Rb contents of the K-feldspar grains being measured in optical dating. Ancient TL 19(2), 43-46.

Jacobs, Z., Roberts, R.G., Galbraith, R.F., Deacon, H.J., Grün, R., Mackay, A., Mitchell, P., Vogelsang, R., Wadley, L., 2008. Ages for the Middle Stone Age of southern Africa: implications for human behavior and dispersal. Science 322(5902), 733-735.

Jain, M., Murray, A.S., Bøtter-Jensen, L., 2003. Characterisation of blue-light stimulated luminescence components in different quartz samples: implications for dose measurement. Radiat. Meas. 37(4-5), 441-449.

Kreutzer, S., Martin, L., Guérin, G., Tribolo, C., Selva, P., Mercier, N., 2018. Environmental dose rate determination using a passive dosimeter: techniques and workflow for alpha-Al2O3: C chips. Geochronometria 45, 56-67.

Kreutzer, S., Tribolo, C., Martin, L., Mercier, N., 2020. Dose-Rate Estimation using Al2O3: C chips: Aftermath. Ancient TL 38, 1-10.

Lamothe, M., Brisson, L.F., Hardy, F., 2020. Circumvention of anomalous fading in feldspar luminescence dating using Post-Isothermal IRSL. Quat. Geochron. 57, 101062.

Lamothe, M., Brisson, L. F., Hardy, F., 2018. Dose recovery performance in double IRSL/pIRIR SAR protocols. Radiat. Meas. 120, 120-123.

Lanos, P., Dufresne, P., 2019. ChronoModel version 2.0 User manual. https://hal.archives-ouvertes.fr/hal-02058018

Lanos, P. and Philippe, A. (2018). Event date model: a robust Bayesian tool for chronology building. Commun. for Stat. Applications and Meth. 25(2):131-157.

Li, B., Roberts, R.G., Jacobs, Z., Li, S.H., Guo, Y.J., 2015. Construction of a 'global standardised growth curve' (gSGC) for infrared stimulated luminescence dating of K-feldspar. Quat. Geochron. 27, 119-130.

Li, B., Jacobs, Z., Roberts, R. G., Galbraith, R., Peng, J., 2017. Variability in quartz OSL signals caused by measurement uncertainties: Problems and solutions. Quat. Geochron. 41, 11-25.

Martin, L., 2015. Caractérisation et modélisation d'objets archéologiques en vue de leur datation par des méthodes paléo-dosimétriques. Simulation des paramètres dosimétriques sous Geant4. PhD thesis, University of Bordeaux Montaigne.

Mejdahl, V., Bøtter-Jensen, L., 1994. Luminescence dating of archaeological materials using a new technique based on single aliquot measurements. Quaternary Sci. Rev. 13(5-7), 551-554.

Millard, A.R., 2006. Bayesian analysis of ESR dates, with application to Border Cave. Quat. Geochron. 1(2), 159-166.

Miller G.H., Beaumont P.B., 1989. Dating the Middle Stone Age at Border Cave, South Africa, by the epimerization of the isoleucine in ostrich eggshells. Bull. Geol. Soc. Am. Abstracts with programs 21, A235.

881 Miller, G.H., Beaumont, P.B., Jull, A.J.T., Johnson, B., 1992. Pleistocene geochronology and the
882 paleothermometry from protein diagenesis in ostrich eggshells: implication for the evolution of
883 modern humans. Aitken M.J., Stringer C.B., and Mellars P.A. (eds.): The origin of modern Humans
884 and the impact of chronometric dating, 149-157. Philos. T. Roy. Soc. B.
885 Miller, G.H., Beaumont, P.B., Jull, A.J.T., Johnson, B., 1993. Pleistocene geochronology and the
886 paleothermometry from protein diagenesis in ostrich eggshells: implication for the evolution of
887 modern humans. In: Aitken, M.J., Stringer, C.B., and Mellars, P.A. (Eds.), The Origin of Modern
888 Humans and the Impact of Chronometric Dating. Princeton University Press, Princeton, pp. 49-
889 68.
890 Miller, G.H., Beaumont, P.B., Deacon, H.J., Brooks, A.S., Hare, P.E., Jull, A.J.T., 1999. Earliest modern
891 humans in southern Africa dated by isoleucine epimerization in ostrich eggshell. Quaternary Sci.
892 Rev. 18, 1537-1548.
893 Murray, A.S., Wintle, A.G., 2000. Luminescence dating of quartz using an improved single-aliquot
894 regenerative-dose protocol. Radiat. Meas. 32, 57-73.
895 Peng, J., Wang, X., Adamiec, G., 2022. The build-up of the laboratory-generated dose-response curve
896 and underestimation of equivalent dose for quartz OSL in the high dose region: A critical
897 modelling study. Quat. Geochron. 67, 101231.
898 Perić, Z.M., Marković, S.B., Filyó, D., Thiel, C., Murray, A.S., Gavrilov, M.B., Nett, J.J., Sipos, G., 2021.
899 Quartz OSL and polymineral post IR-IRSL dating of the Požarevac loess-palaeosol sequence in
900 north-eastern Serbia. Quat. Geochron. 66, 101216.
901 Philippe, A., Guérin, G., Kreutzer, S., 2019. BayLum-An R package for Bayesian analysis of OSL ages: An
902 introduction. Quat. Geochron. 49, 16-24.
903 Prescott, J.R., Hutton, J.T., 1994. Cosmic ray contributions to dose rates for luminescence and ESR
904 dating: large depths and long-term time variations. Radiat. Meas. 23, 497-500.
905 Rees-Jones, J., 1995. Optical dating of young sediments using fine-grain quartz. Ancient TL 13(2), 9-14.
906 Rhodes, E. J., Ramsey, C. B., Outram, Z., Batt, C., Willis, L., Dockrill, S., Bond, J., 2003. Bayesian methods
907 applied to the interpretation of multiple OSL dates: high precision sediment ages from Old
908 Scatness Broch excavations, Shetland Isles. Quaternary Sci. Rev. 22(10-13), 1231-1244.
909 Roberts, H. M., Duller, G.A., 2004. Standardised growth curves for optical dating of sediment using
910 multiple-grain aliquots. Radiat. Meas. 38(2), 241-252.
911 Sievers, C., Backwell, L., d'Errico, F., Wadley, L., 2022. Plant bedding construction between 60,000 and
912 40,000 years ago at Border Cave, South Africa. Quaternary Sci. Rev. 275: 107280.
913 Singhvi, A.K., Stokes, S.C., Chauhan, N., Nagar, Y.C., Jaiswal, M.K., 2011. Changes in natural OSL
914 sensitivity during single aliquot regeneration procedure and their implications for equivalent
915 dose determination. Geochronometria 38(3), 231-241.
916 Singhvi, A.K., Rajapara, H.M., Garnett, S., Chauhan, N., Gajjar, P.N., Wasson, R.J., 2021. How robust are
917 SAR single grain paleodoses: the role of sensitivity changes? LED 2021, 13-17th September 2021.
918 Ancient TL 39, S.
919 Steffen, D., Preusser, F., Schlunegger, F., 2009. OSL quartz age underestimation due to unstable signal
920 components. Quat. Geochron. 4(5), 353-362.
921 Stratford, D., Clark, J., Wojcieszak, M., de la Peña, P., Wadley, L., d'Errico, F., Mauran, G., Sievers, C.,
922 Banks, W., Beard, T., Horn, M., Shadrach, K., Morrissey, P., Backwell, L., 2022. Geoarchaeology
923 and zooarchaeology of Border Cave, South Africa: initial multiproxy considerations of
924 stratigraphy and site formation processes from the Backwell et al. excavations. Quaternary Sci.
925 Rev. 291: 107618.
926 Thomsen, K., Murray, A.S., Buylaert, J.P., Jain, M., Hansen, J.H., Aubry, T., 2016. Testing single-grain
927 quartz OSL methods using sediment samples with independent age control from the Bordes-
928 Fitte rockshelter (Roches d'Abilly site, Central France). Quat. Geochron. 31, 77-96.
929 Thomsen, K.J., Murray, A., Jain, M., 2012. The dose dependency of the over-dispersion of quartz OSL
930 single grain dose distributions. Radiat. Meas. 47(9), 732-739.
931 Tribolo, C., Mercier, N., Douville, E., Joron, J.-L., Reyss, J.-L., Rufer, D., Cantin, N., Lefrais, Y., Miller, C.E.,
932 Parkington, J., Porraz, G., Rigaud, J.-P., Texier, P.-J, 2013. OSL and TL dating of the Middle Stone

Age sequence of Diepkloof Rock Shelter (Western Cape, South Africa): a clarification. J. Archaeol. Sci. 40 (9), 3401-3411.
Tribolo, C., Asrat, A., Bahain, J.-J., Chapon, C., Douville, E., Fragnol, C., Hernandez, M., Hovers, E., Leplongeon, A., Martin, L., Pleurdeau, D., Pearson, O., Puaud, S., Assefa, Z., 2017. When the Rains Stopped: Geochronological and Sedimentological Evidence for the Middle and Later Stone Age Sequence of Goda Buticha, Southeastern Ethiopia. PlosOne 12(1), e0169418.
Tsukamoto, S., Murray, A.S., Huot, S., Watanuki, T., Denby, P.M., Bøtter-Jensen, L., 2007. Luminescence property of volcanic quartz and the use of red isothermal TL for dating tephras. Radiat. Meas. 42(2), 190-197.
Villa, P., Soriano, S., Tsanova, T., Degano, I., Higham, T.F., d'Errico, F., Backwell, L.R., Lucejko, J., Beaumont, P.B., 2012. Border cave and the beginning of the Later Stone Age in South Africa. P. Natl. Acad. Sci. USA. 109(33), 13208-13213.
Vogel, J.C., Beaumont, P.B., 1972. Revised radiocarbon chronology for the Stone Age in South Africa. Nature 237(5349), 50-51.
Yoshida, H., Roberts, R.G., Olley, J.M., Laslett, G.M., Galbraith, R.F., 2000. Extending the age range of optical dating using single 'supergrains' of quartz. Radiat. Meas. 32(5-6), 439-446.
Wadley, L., 2015. Those marvellous millennia: the Middle Stone Age of southern Africa. Azania 50(2), 155-226.

Author contributions

CT, NM, DS, LW, LB, FD conducted the sampling. CT, CD and NM conducted the luminescence dating measurements. NC conducted the XRD analyses. WEB made the Bayesian modeling and calculations and wrote the corresponding section. DS made Figure 1. CT wrote the manuscript. All authors commented, corrected, and approved the final manuscript.

Declaration of competing interest

The authors declare that they have no competing financial interests or personal relationships that could have influenced the work reported in this paper.